Article

Developmental Cell

Localized glucose import, glycolytic processing, and mitochondria generate a focused ATP burst to power basement-membrane invasion

Graphical abstract

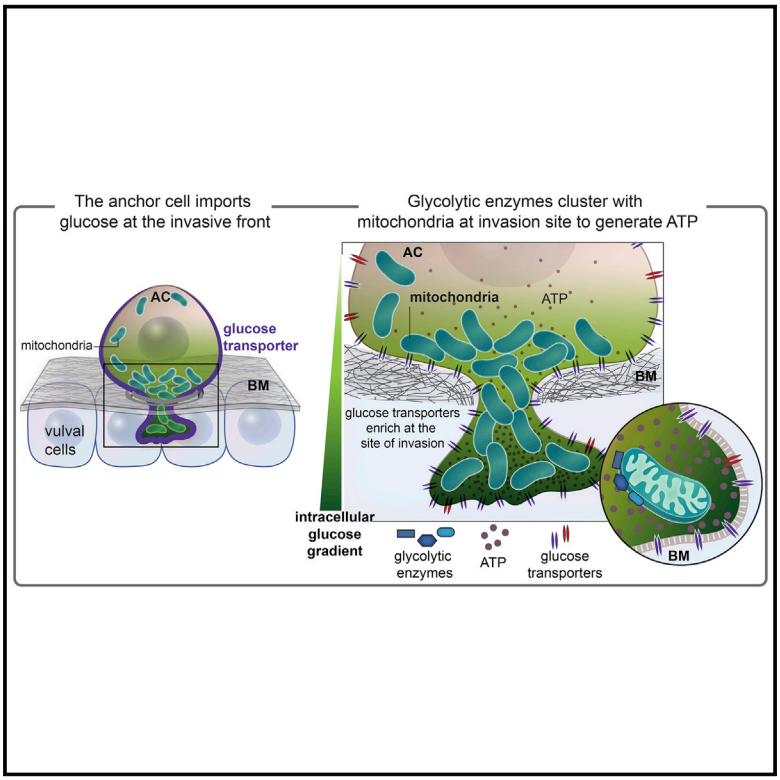

Highlights

- Cell invasion through basement membrane is accompanied by a transient ATP burst
- Two distinct glucose transporters localize to the invasive front to fuel ATP synthesis
- Glycolytic enzymes cluster with mitochondria at the invasion site for ATP production
- Energy import, processing, and generation are interlinked with the invasive machinery

Authors

Aastha Garde, Isabel W. Kenny, Laura C. Kelley, Qiuyi Chi, Ayse Sena Mutlu, Meng C. Wang, David R. Sherwood

Correspondence

david.sherwood@duke.edu

In brief

Cell invasion through basement membrane is energy intensive. Garde et al. identify two glucose transporters that polarize to the invasive front of the anchor cell in *Caenorhabditis elegans* and import glucose to fuel a burst of mitochondrially generated ATP that powers the invasive protrusions that breach basement membrane.

Garde et al., 2022, Developmental Cell *57*, 732–749
March 28, 2022
https://doi.org/10.1016/j.devcel.2022.02.019

CellPress

CellPress

Developmental Cell

Article

Localized glucose import, glycolytic processing, and mitochondria generate a focused ATP burst to power basement-membrane invasion

Aastha Garde,[1,2] Isabel W. Kenny,[1] Laura C. Kelley,[1] Qiuyi Chi,[1] Ayse Sena Mutlu,[3] Meng C. Wang,[3,4] and David R. Sherwood[1,5,*]

[1]Department of Biology, Duke University, Box 90338, Durham, NC 27708, USA
[2]Department of Cell Biology, Duke University Medical Center, Durham, NC 27708, USA
[3]Huffington Center on Aging, Baylor College of Medicine, Houston, TX 77030, USA
[4]Howard Hughes Medical Institute, Baylor College of Medicine, Houston, TX 77030, USA
[5]Lead contact
*Correspondence: david.sherwood@duke.edu
https://doi.org/10.1016/j.devcel.2022.02.019

SUMMARY

Invasive cells use transient, energy-consuming protrusions to breach basement membrane (BM) barriers. Using the ATP sensor PercevalHR during anchor cell (AC) invasion in *Caenorhabditis elegans*, we show that BM invasion is accompanied by an ATP burst from mitochondria at the invasive front. RNAi screening and visualization of a glucose biosensor identified two glucose transporters, FGT-1 and FGT-2, which bathe invasive front mitochondria with glucose and facilitate the ATP burst to form protrusions. FGT-1 localizes at high levels along the invasive membrane, while FGT-2 is adaptive, enriching most strongly during BM breaching and when FGT-1 is absent. Cytosolic glycolytic enzymes that process glucose for mitochondrial ATP production cluster with invasive front mitochondria and promote higher mitochondrial membrane potential and ATP levels. Finally, we show that UNC-6 (netrin), which polarizes invasive protrusions, also orients FGT-1. These studies reveal a robust and integrated energy acquisition, processing, and delivery network that powers BM breaching.

INTRODUCTION

Basement membrane (BM) is a dense, cross-linked, planar extracellular matrix (ECM) that underlies or surrounds most tissues (Jayadev and Sherwood, 2017; Pozzi et al., 2017). Although BMs pose a barrier to cell migration, many cells acquire a specialized ability to breach BMs to carry out important developmental and physiological processes. These include cytotrophoblasts that penetrate uterine-wall BM to implant, sensory neurons that extend pioneering axons through BM into the spinal cord, neural crest cells that breach BM to leave the neural tube, and leukocytes that transmigrate BM to enter and exit tissues during immune surveillance (Leonard and Taneyhill, 2020; Moser et al., 2018; Nichols and Smith, 2019; Schwartz et al., 2021). Dysregulated cell invasion also underlies diseases such as the pregnancy disorder pre-eclampsia, premature skull bone fusion in craniosynostosis, rheumatoid arthritis, and cancer metastasis (Al-Rekabi et al., 2017; Fisher, 2015; Reuten et al., 2021; Xing et al., 2016). Understanding the mechanisms that allow cells to traverse BMs is thus of both basic and clinical importance.

Cell-invasion events are often stochastic and occur deep within tissues and are therefore difficult to experimentally dissect *in vivo* (Kelley et al., 2014). As a result, most studies on BM invasion have been carried out using artificial matrices on 2D surfaces that mimic planar BMs (Cambi and Chavrier, 2021; Ezzoukhry et al., 2018). These experiments have identified invadosomes, which are force producing, F-actin-based membrane protrusions that bind to and proteolytically degrade ECM (Paterson and Courtneidge, 2018). Often referred to as podosomes in normal cells and invadopodia in cancer cells, these invasive structures are likely a related continuum of membrane-associated protrusions that alter their dynamics, arrangements, and composition in response to the environment (Di Martino et al., 2016; Hastie and Sherwood, 2016; Paterson and Courtneidge, 2018). Confirming their importance, invadosomes have been observed in many matrix-degrading cell types *in vivo*, such as pioneering axons, remodeling neuromuscular junctions, and isolated tumor cells (Chan et al., 2020; Chen et al., 2019; Nichols and Smith, 2019). While the mechanisms that build and modulate invadosomes are being resolved, it is unknown how cells metabolically support these energy- demanding protrusive structures (Garde and Sherwood, 2021). F-actin turnover, protease trafficking, and dynamic membrane addition at invadosomes are high ATP-consuming processes (Li et al., 2019; Marshansky and Futai, 2008; Shah et al., 2015). Recent studies

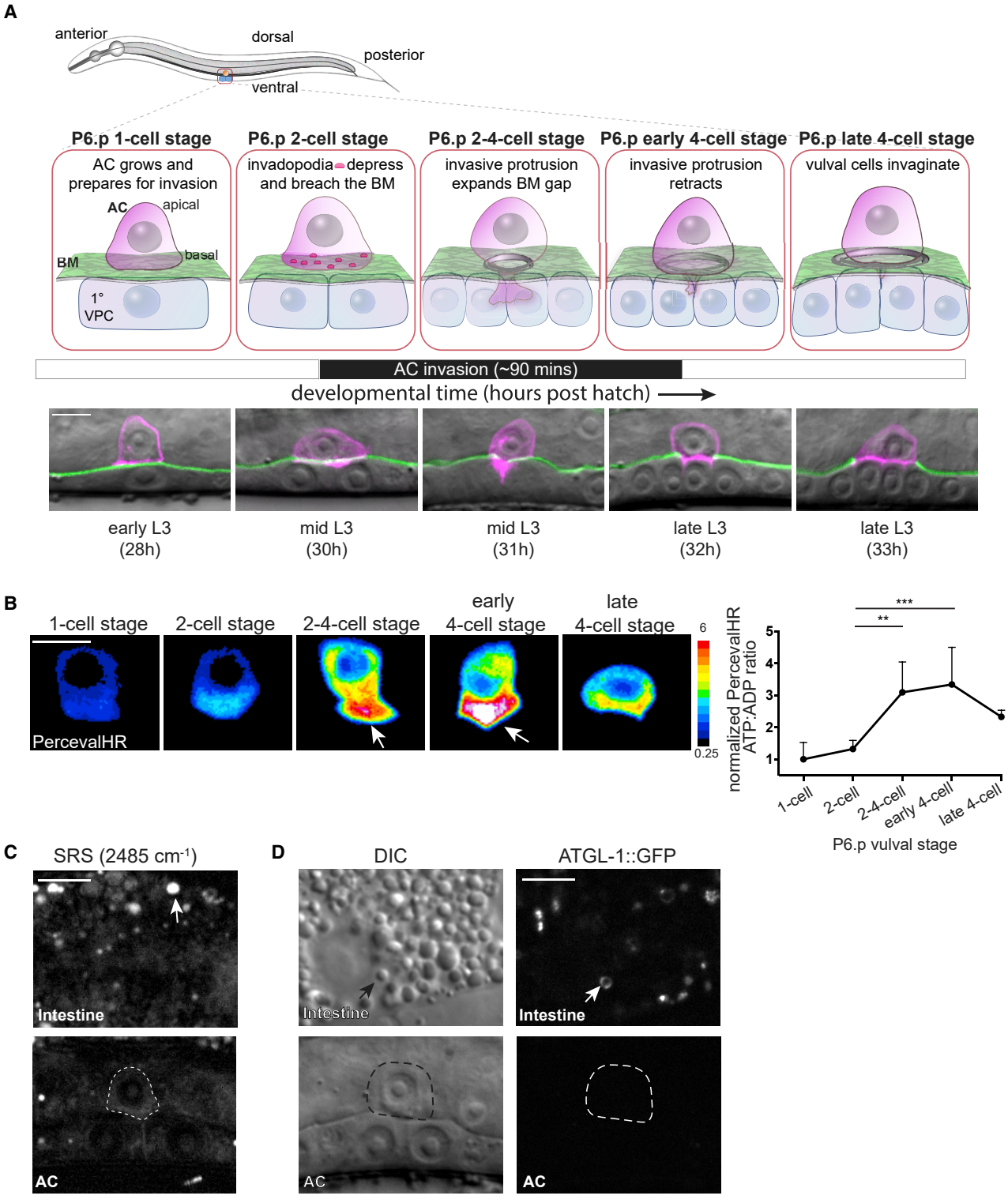

Figure 1. A transient surge in the ATP:ADP ratio at the invasive front accompanies AC-BM invasion

(A) A timeline of AC (magenta) invasion through BM (green) in *C. elegans* (top, schematic of lateral view; bottom, micrographs of lateral view of AC membrane labeled by *cdh-3p::mCherry::PLCδ^{PH}* and BM labeled by *laminin::GFP*) from the P6.p 1-cell stage of the 1° vulval precursor cells (VPCs, differential interference contrast [DIC], gray) to the P6.p late 4-cell stage.

(B) (Left) Spectral fluorescence intensity maps of the ATP:ADP ratio in the AC visualized by the ATP:ADP ratiometric sensor PercevalHR (*lin-29p::PercevalHR*) before (P6.p 1-cell and 2-cell stage), during (P6.p 2–4-cell and early 4-cell stage), and after BM breaching (P6.p late 4-cell stage). ATP:ADP ratios are highest at the

(legend continued on next page)

have found that mitochondria localize to the leading edge of pancreatic, prostate, ovarian, and glioblastoma cancer cells, where they are thought to provide localized ATP to fuel F-actin polymerization, actomyosin contractility, and cell-matrix adhesions required for cell movement (Caino et al., 2015; Cunniff et al., 2016; Papalazarou et al., 2020; Rivadeneira et al., 2015). Whether localized mitochondria and ATP support invadosomes during BM breaching, and how cells supply a carbon source to fuel localized mitochondria are unknown.

Anchor cell (AC) invasion in *C. elegans* is a highly stereotyped and experimentally accessible model of cell invasion (Sherwood and Sternberg, 2003). The AC is a specialized uterine cell that invades the underlying uterine and vulval BMs to initiate uterine-vulval connection. The AC breaches the BM with dynamic invadosomes, which have been termed invadopodia because of their similar protrusive nature to cancer cell invadopodia (Hagedorn et al., 2013). Numerous AC invadopodia rapidly form and disassemble prior to invasion and are polarized to the AC-BM interface by UNC-6 (netrin), a cue secreted by the underlying vulval cells (Hagedorn et al., 2014; Naegeli et al., 2017; Wang et al., 2014a; Ziel et al., 2009). When an invadopodium breaches the BM, a large protrusion forms at the site via exocytosis of lysosomes, which widens the BM opening through proteolytic degradation and physical displacement (Naegeli et al., 2017). Mitochondria and ATP polarize to the invasive front of the AC, where they are implicated in promoting a nonproteolytic, adaptive form of BM invasion (Kelley et al., 2019). Like cancer cells, however, the role of localized mitochondria and ATP production in supporting the normal BM invasive machinery is unclear, as is the source of fuel for localized mitochondria.

Using the genetically encoded ATP biosensor PercevalHR, we show that ATP levels at the AC's invasive front dramatically increase during BM breaching. To understand how this ATP burst is fueled, we conducted an RNAi screen of carbohydrate, lipid, and amino-acid transporters, and found that FGT-1, a facilitated glucose transporter, is required for normal invasion. Endogenous tagging revealed that FGT-1 enriches at the AC's invasive plasma membrane and that, like the BM breaching protrusive machinery, FGT-1 is polarized by UNC-6 (netrin). A glucose biosensor showed that FGT-1 polarization facilitates an intracellular gradient of glucose that bathes the invasive front mitochondria with high glucose and supports increased ATP production, which promotes invasive protrusion formation. We further discovered that glycolytic enzymes, which breakdown glucose to fuel mitochondrial ATP production, cluster in puncta that co-localize with mitochondria at the invasive front and that these mitochondria have increased membrane potential for ATP production. Finally, through a sensitized genome-scale RNAi screen, we identified FGT-2, another glucose transporter, that specifically increases its enrichment at the invasive membrane during BM breaching and enhances glucose import and peak ATP generation. We also identified the mitochondrial adaptor TRAK-1 and the O-GlcNAc transferase OGT-1, which have been shown to arrest mitochondria in the presence of high glucose and found that they function to concentrate mitochondria at the glucose-rich invasive front. Together, these results reveal a localized glucose uptake, breakdown, and, mitochondrial ATP delivery system that both powers the BM invasive machinery and is itself an integrated component of that machinery.

RESULTS

BM invasion is accompanied by an ATP burst from mitochondria at the invasive front

BM transmigration by the AC is a highly stereotyped cell-invasion event (Sherwood and Sternberg, 2003). The uterine AC invades over a specific ~90-min window during the L3 larval stage that correlates with the divisions of the underlying 1° fated vulval precursor cells (VPCs) (Figure 1A). The AC is specified and grows in size during the early L3 larval stage (VPC P6.p 1-cell to 2-cell stage) and begins breaching the BM during the mid-L3 larval stage (P6.p 2-cell stage) using dynamic invadopodia that penetrate the BM (Hagedorn et al., 2014). Once an invadopodium penetrates the BM, F-actin polymerization is enriched at the site of the BM breach and a single large protrusion forms, clearing a wide opening in the BM during the period between the P6.p 2–4-cell and early P6.p 4-cell stage (Naegeli et al., 2017). The AC completes invasion before the late P6.p 4-cell stage and attaches to the central VPCs, which initiates the uterine-vulval connection (Figure 1A). Through analysis of mitochondria localization and the use of the ATP sensor ATeam, we previously showed that mitochondria and ATP enrich at the invasive front of the AC during BM breaching (Kelley et al., 2019). Whether ATP levels are specifically increased at the time of invasion to facilitate BM breaching, however, is unknown.

To examine ATP levels over the course of AC invasion, we used the ratiometric biosensor PercevalHR (Tantama et al., 2013). PercevalHR consists of a circularly permuted fluorophore (cpmVenus), fused to the bacterial ATP-binding protein GlnK. ATP and ADP compete for binding to GlnK, and each binding state has a unique excitation spectrum, allowing the cytosolic ATP:ADP ratio to be determined (STAR Methods; Figures S1A and S1B). The ATP:ADP ratio calculated using PercevalHR is independent of the concentration of the sensor, which allows robust temporal analysis of ATP dynamics. An increase in the ratio is a strong indicator of greater ATP production and reflects the free energy of ATP hydrolysis available for driving energy-demanding processes (Tantama et al., 2013). Ratiometric

invasive side of the AC (arrows) during BM breaching. This and all subsequent color bars show a spectral representation of fluorescence intensity displaying the minimum and maximum pixel value range of the acquired data. The numbers represent minimum and maximum pixel intensity where all images within a panel are shown with the same constrained ranges. Where hi-lo is shown in subsequent figures, the spectral range for each image was set independently to highlight apical over basal fluorescence enrichment differences within the AC (see STAR Methods). (Right) Quantification of total ATP:ADP ratio over developmental time ($n \geq 5$ ACs per time point, mean + SEM, ** $p < 0.01$, *** $p < 0.001$, one-way ANOVA with *post hoc* Tukey's test).

(C) Visualization of CH_2 bonds in lipids using stimulated Raman scattering (SRS) microscopy images at 2,485 cm^{-1} during the P6.p 2-cell stage shows lipid droplets in intestinal cells (top, arrow) and no lipid droplets in the AC (bottom, dotted line outlines AC; n = 8 animals imaged).

(D) An ATGL-1::GFP translational reporter localizes to lipid droplets in the intestine (top, arrow). No lipid droplets are apparent in the AC at the P6.p 2-cell stage (bottom, dotted lines outline AC; n = 11 animals imaged).

Scale bars: 5 μm. See also Figure S1.

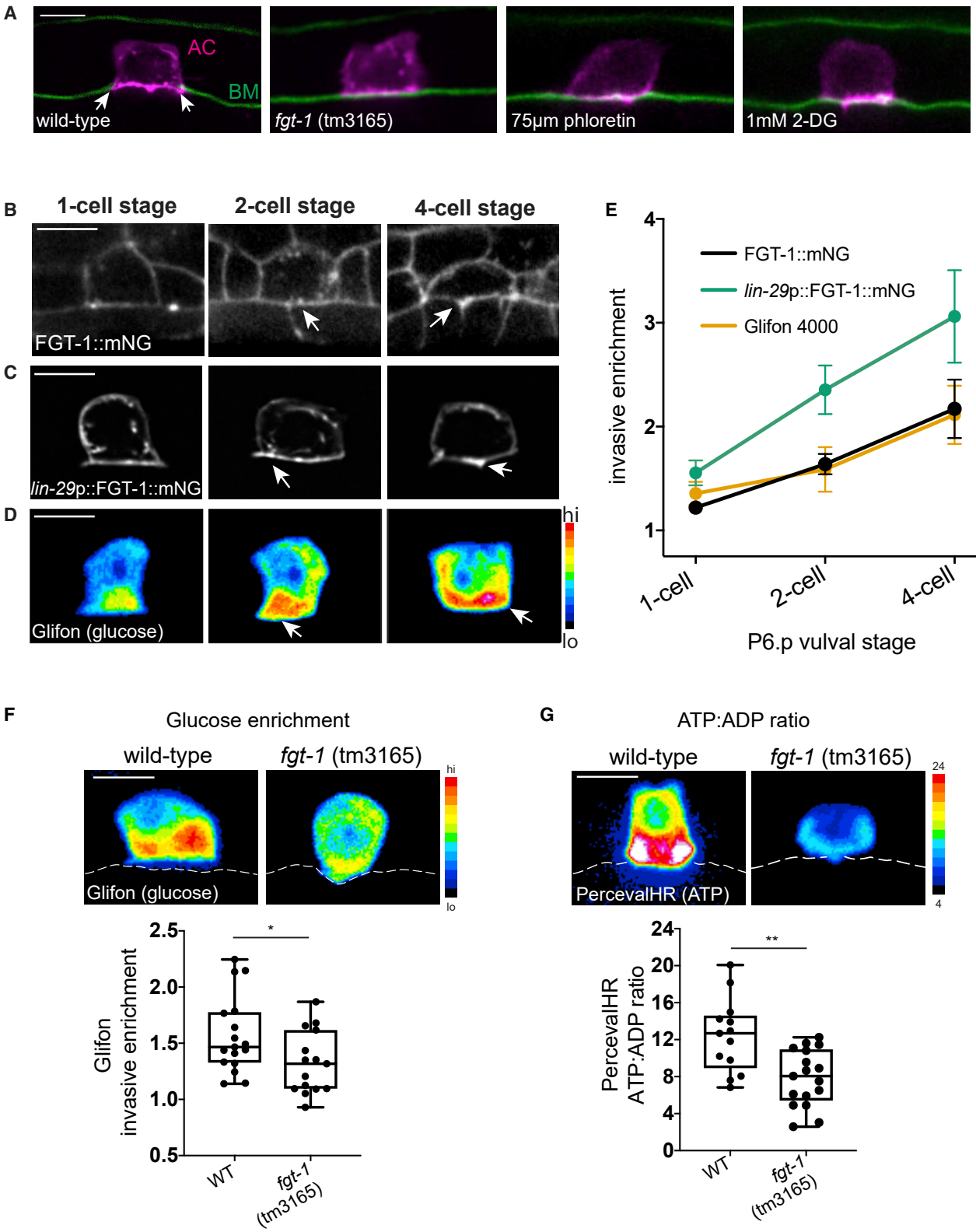

Figure 2. Invasive membrane-enriched FGT-1 and localized glucose import promote ATP production and BM invasion

(A) Representative AC (magenta) invasion phenotypes in wild-type, *fgt-1 (tm3165)* null mutant, phloretin-treated, and 2-DG-treated animals at the P6.p late 4-cell stage. Arrows indicate BM (green) breach in a wild-type animal.

(B) Endogenous FGT-1 (*fgt-1::mNG*) distribution in the AC over developmental time. Arrows indicate regions of FGT-1 enrichment.

(legend continued on next page)

imaging of AC-expressed PercevalHR (*lin-29p::PercevalHR*) revealed an ATP:ADP ratio gradient that was ~75% greater at the invasive basal side of the AC compared with the apical side during BM breaching (Figures 1B and S1A). Examination of PercevalHR prior to (P6.p 1-cell and 2-cell stages), during (P6.p 2–4-cell and early 4-cell stages), and after (P6.p late 4-cell stage) invasion, also revealed a transient 2.5-fold increase in the ATP:ADP ratio during BM clearance (Figure 1B). Furthermore, cytosolic GFP, driven by the same promoter as PercevalHR, showed that while cytosolic GFP fluorescence increased slowly during AC invasion, the ADP signal remained constant and the ATP signal rapidly doubled during BM breaching (Figures S1B and S1C). To verify that gradients of pH in the AC did not impact PercevalHR's readout of ATP:ADP ratios, we examined cytosolic GFP (pKa 6.0), whose fluorescence can be quenched by low pH and mCherry whose fluorescence is insensitive to low pH. GFP and mCherry had similar uniform fluorescence in the cytoplasm (Figure S1D), indicating the absence of a low-pH domain in the cytoplasm of the AC (Shinoda et al., 2018). Similarly, the pH biosensor Rosella (Rosado et al., 2008, see STAR Methods) also demonstrated the absence of a low-pH domain in the AC (Figure S1E). Together, these observations indicate that the AC dramatically increases cytosolic ATP levels at the site of invasion during BM breaching.

The facilitated glucose transporter FGT-1 promotes AC invasion

How cells acquire carbon sources to fuel the energy-intensive process of invasion through ECM is not well understood (Garde and Sherwood, 2021). We hypothesized that the rapid increase in the ATP:ADP ratio during BM invasion could be due to catabolism of either an intracellular nutrient store or an imported fuel source. Lipid droplets are a cytoplasmic storage organelle for neutral lipids that can be oxidized to fuel ATP production (Rambold et al., 2015). Using label-free stimulated Raman scattering (SRS) microscopy (Mutlu et al., 2021), we visualized CH_2 bonds that are abundant in the fatty-acid chains of neutral lipids stored in lipid droplets. Unlike the intestine, the main fat-storage tissue of *C. elegans*, the AC did not have any lipid droplets prior to or during invasion (N = 0/8) (Figure 1C). In addition, we examined a GFP-tagged lipid-droplet-resident protein ATGL-1 (ATGL-1::GFP), and found abundant lipid droplets in intestinal cells, but none in the AC (N = 0/11; Figure 1D).

Given the lack of an internal lipid store, we examined whether the AC imports a nutrient source to fuel rapid ATP production. Using an AC-specific RNAi knockdown strain (STAR Methods), we targeted 35 genes encoding proteins involved in transmembrane transport of lipids, amino acids, and hexose sugars (Table S1). We predicted that reduction of a carbon source catabolized for ATP production would perturb AC invasion. AC invasion was scored at the late P6.p 4-cell stage, ~45 min after wild-type ACs complete invasion. RNAi-mediated knockdown of only one gene, *fgt-1*, resulted in significant AC invasion defects, where ~35% of AC invasions failed (Table S1). The *fgt-1* gene encodes the only known functional *C. elegans* homolog of mammalian glucose transporters (GLUTs), which are 12-pass transmembrane proteins that facilitate bidirectional, passive transport of glucose down concentration gradients (Feng et al., 2013; Kitaoka et al., 2013). Animals harboring a *fgt-1*-null allele (*tm3165*) had an invasion defect (~30%) similar to *fgt-1* RNAi (Figure 2A; Table S1). Examination of invasion in *fgt-1* mutant animals at the time of invasion initiation (P6.p 2–4-cell stage) revealed a highly penetrant invasion-initiation delay (86%), although most *fgt-1* mutants completed invasion by the P6.p 6-cell stage (~9% defective) (Figure S2A; Table S2).

To further verify that GLUT transporters and glucose function in promoting invasion, animals were treated prior to AC invasion with 100 μM phloretin, a pharmacological GLUT inhibitor. Supporting a role for glucose transport in AC invasion, inhibition of GLUTs perturbed invasion (Figure 2A; Table S1). Glucose metabolism was impaired by culturing worms on a low dose of the nonmetabolizable glucose ortholog 2-deoxyglucose (2-DG), which also inhibited invasion (Figure 2A; Table S1). Taken together, these observations suggest that both glucose transport and glucose metabolism facilitate AC invasion and that imported glucose might fuel heightened ATP generation during BM breaching.

FGT-1 and glucose enrichment at invasive front elevates ATP levels during invasion

Next, we investigated how FGT-1 protein and glucose transport are localized and contribute to increased ATP levels during BM invasion. We used CRISPR-Cas9-mediated genome editing to endogenously tag FGT-1 (*fgt-1::mNG*). FGT-1::mNG was broadly localized to the plasma membrane of cells throughout the animal, including the AC and its neighboring uterine and vulval cells. Notably, FGT-1::mNG was uniquely polarized to the basal invasive plasma membrane of the AC (Figures 2B and 2E), compared with its neighboring noninvasive uterine cells (Figure S2B). To visualize FGT-1::mNG polarity within the AC without membrane signal from neighboring cells, FGT-1 was expressed under an AC-specific promoter (*lin-29p::fgt-1::mNG*). AC-specific expression revealed FGT-1 enrichment at the invasive cell

(C) AC-specific FGT-1 (*lin-29p::fgt-1::mNG*) distribution in the AC over developmental time. Arrows indicate regions of FGT-1 enrichment.
(D) Spectral fluorescence-intensity maps of glucose distribution in the AC over developmental time visualized by the glucose sensor Green Glifon 4000 (*lin-29p*::Glifon 4000). Glucose levels were highest in the invading side of the AC (indicated by arrows).
(E) Quantification of invasive enrichment of endogenous FGT-1 (black), AC-specific FGT-1 (green), and Green Glifon 4000 (gold) in the AC over developmental time ($n \geq 5$ ACs for each timepoint, mean ± SEM).
(F) (Top) glucose distribution (*lin-29p*::Glifon 4000) in the ACs of a wild-type and *fgt-1* mutant animal during invasion. BM position (from DIC image, not shown), dotted line. (Bottom) Quantification of invasive enrichment of Green Glifon 4000 signal (ACs imaged and quantified at the P6.p 2–4-cell and early 4-cell stages, boxplot, $n \geq 15$ per genotype, * $p < 0.05$, unpaired two-tailed t test).
(G) (Top) ATP:ADP ratio (*lin*-29p::PercevalHR) in the ACs of a wild-type and *fgt-1* mutant animal during invasion. BM position (from DIC image not shown), dotted line. (Bottom) Quantification of ATP:ADP ratio (ACs imaged and quantified at the P6.p 2–4-cell and early 4-cell stages, boxplot, $n \geq 13$ per genotype, ** $p < 0.01$, unpaired two-tailed t test).
Scale bars: 5 μm.
See also Figure S2.

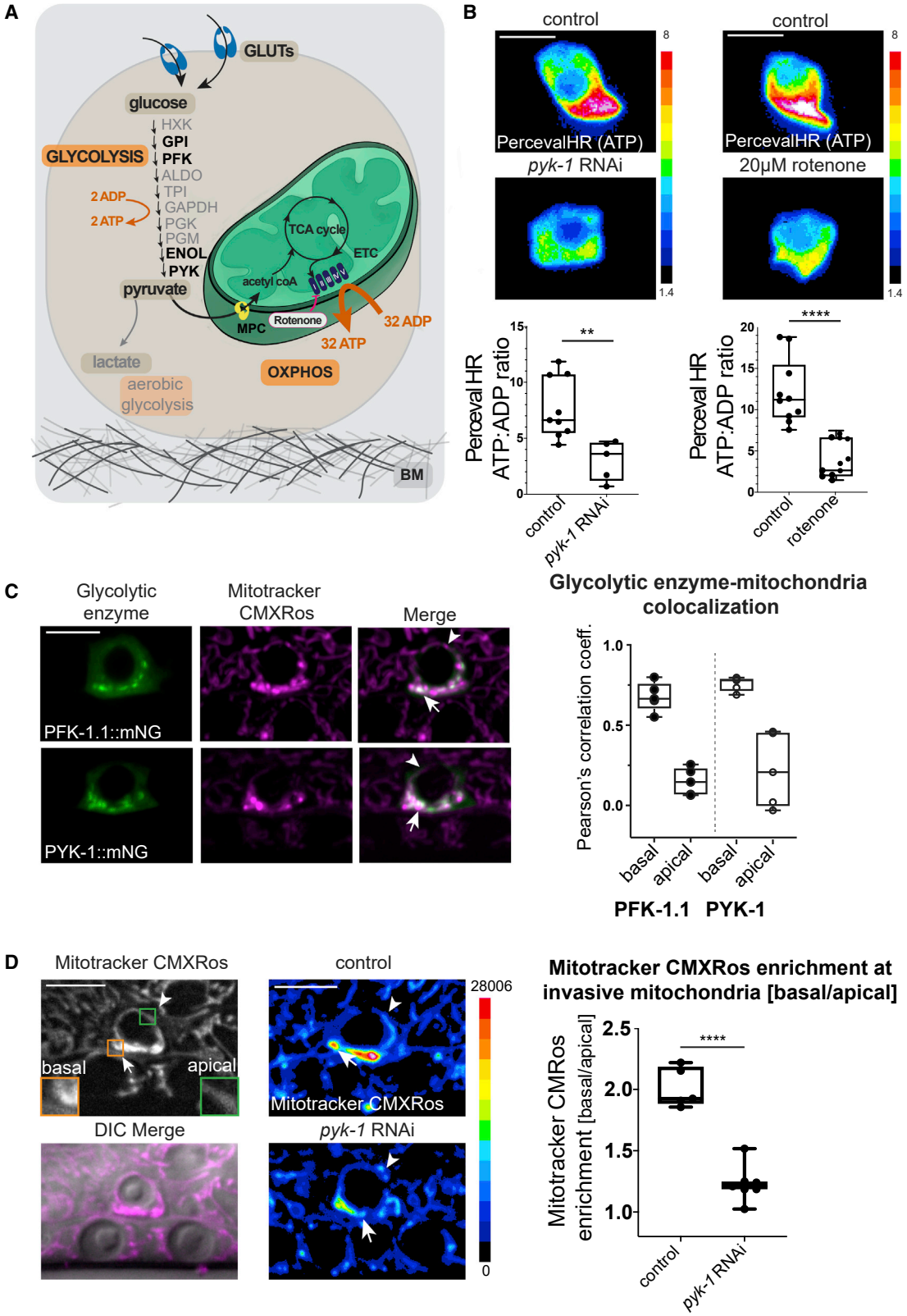

(legend on next page)

membrane beginning at the P6.p 1-cell stage and increasing to the time of invasion, reaching 2-fold greater levels at the invasive plasma membrane compared with the apical membrane at the time of invasion (Figures 2C and 2E). Due to the passive and bidirectional transport of glucose through GLUT-family transporters, we hypothesized that FGT-1 enrichment could facilitate local glucose import. To visualize intracellular glucose, we expressed the genetically encoded glucose biosensor Green Glifon 4000 in the AC (*lin-29p::Green Glifon 4000*). Green Glifon 4000 is composed of fluorescent protein Citrine fused to the bacterial glucose- and galactose-binding protein MglB. Green Glifon 4000 undergoes a conformational change and subsequent increase in fluorescence intensity in response to glucose binding (Mita et al., 2019). Supporting a functional role for enriched FGT-1 localization, Green Glifon 4000 signal was also enriched at the invasive region of the AC by the P6.p 1-cell stage, and its concentration further increased until the time of BM breaching (Figures 2D and 2E). These findings indicate that localized FGT-1 may facilitate import of glucose to the site of BM breach.

To determine whether FGT-1 enables polarized glucose import, we examined *fgt-1*null mutants expressing Green Glifon 4000. Wild-type ACs had an ~2-fold glucose enrichment at the invasive front during BM breaching (P6.p 2–4-cell and early 4-cell stages). In contrast, *fgt-1* mutants had a reduction of ~25% in glucose enrichment at the ACs' invasive side during BM breaching (Figures 2F and S2C). Finally, we examined if FGT-1 is required for the increase in ATP:ADP ratio during AC invasion. Consistent with this notion, the ATP:ADP ratio was ~40% lower in *fgt-1* mutant animals during BM breaching (Figure 2G). These results indicate that FGT-1 promotes polarized glucose import, which is required for increased ATP levels during BM breaching.

Oxidative phosphorylation drives increased ATP production during invasion

We next examined how imported glucose is used by the AC to generate ATP during invasion. Most ATP in cells is produced by mitochondrial oxidative phosphorylation (OXPHOS) (Bonora et al., 2012). Prior to entering the mitochondria, glucose is metabolized into pyruvate by glycolysis, a process catalyzed by 10 enzymatic steps in the cytoplasm that generates two molecules of ATP per molecule of glucose (Figure 3A). Cytoplasmic pyruvate can be transported into mitochondria by mitochondrial pyruvate carriers (MPCs) (Bricker et al., 2012; Herzig et al., 2012) to be oxidized by the tricarboxylic acid (TCA) cycle. The electrons produced by glycolysis and the TCA cycle flow through electron carriers, i.e., the electron-transport chain (ETC) in the mitochondrial inner membrane and set up a proton gradient that helps create a membrane potential across the inner mitochondrial membrane. This membrane potential is harnessed for ATP production, with the overall process termed OXPHOS. Some cancer cells, however, rely on glycolysis followed by reduction to lactate as their primary mode of ATP production in aerobic conditions in a process called aerobic glycolysis (Chen et al., 2015).

To determine whether the AC uses aerobic glycolysis or OXPHOS to generate the bulk of ATP for invasion, we impaired cytosolic glycolytic enzymes and the import of pyruvate into the mitochondria for OXPHOS. We hypothesized that if the AC relied primarily on aerobic glycolysis, impairing glycolysis alone would hinder invasion, while the knockdown of pyruvate import would not affect invasion. However, if the AC required OXPHOS, impairing glycolysis and pyruvate import would both impair AC invasion. AC-specific RNAi knockdown of the glycolytic enzyme glucose-6-phosphate isomerase *gpi-1* (the sole *C. elegans* ortholog) and the mitochondrial pyruvate carrier *mpc-2* both perturbed AC invasion (Table S1), strongly suggesting that mitochondrial OXPHOS produces the ATP to fuel BM breaching.

To further test the idea that the AC generates ATP from glucose-fueled OXPHOS, we examined the impact of impairing glycolysis and OXPHOS on ATP production. The RNAi knockdown of a rate-limiting glycolytic enzyme pyruvate kinase (*pyk-1*) dramatically decreased the ATP:ADP ratio at the time of BM breaching (~60% reduction; Figure 3B). Inhibition of OXPHOS with the ETC Complex I inhibitor rotenone similarly reduced the ATP:ADP ratio (~66%) during invasion (Figure 3B). These results indicate that pyruvate generated by glycolysis is used by mitochondria to drive OXPHOS and fuel ATP production during AC invasion.

Glycolytic enzymes co-localize with highly active mitochondria at the invasive front

Although glycolytic enzymes are primarily found throughout the cytosol of cells, they have been shown to concentrate at

Figure 3. Invasive front mitochondria have a high membrane potential, co-localize with glycolytic enzyme clusters, and produce ATP via OXPHOS

(A) A schematic of glucose metabolism in eukaryotic cells including glucose import into the cytoplasm, glucose processing by glycolytic enzymes, import of pyruvate into mitochondria, and its conversion to acetyl CoA, the tricarboxylic acid (TCA) cycle, mitochondrial ATP production via OXPHOS, and rotenone inhibition of complex I of the electron-transport chain (ETC).

(B) (Top) ATP:ADP ratio (*lin-29p*::PercevalHR) in the ACs of empty vector control (L4440) and *pyk-1* RNAi-treated animals (left), and control (DMSO) and rotenone-treated animals (right) during invasion. (Bottom) Quantification of ATP:ADP ratio in ACs of empty vector and *pyk-1* RNAi-treated (left, boxplots, $n \geq 5$ per condition; ** $p < 0.01$, unpaired two-tailed t test) and control and rotenone-treated animals (right, all ACs imaged and quantified at the P6.p 2–4-cell and early 4-cell stages, boxplots, $n \geq 10$ per condition, **** $p < 0.0001$, unpaired two-tailed t test).

(C) (Left) Colocalization of punctate signal of glycolytic enzymes PFK-1.1 and PYK-1A (*lin-29p::pfk-1.1::mNG* and *lin-*29p::*pyk-1a::mNG*, green) and mitochondria stained with Mitotracker CMXRos (magenta) at the invasive side of the AC. Arrows indicate glycolytic enzyme puncta that co-localize with basal mitochondria; arrowheads show apical mitochondria with no glycolytic enzyme colocalization in merged images. (Right) Quantification of Pearson's correlation coefficient between glycolytic enzymes PFK-1.1 and PYK-1A and mitochondria at the basal and apical regions of the AC (ACs imaged and quantified during invasion at the P6.p 2–4-cell and early 4-cell stages, boxplot, n = 5 for each enzyme).

(D) (Left) Mitotracker CMXRos-stained ACs (top, fluorescence; bottom, DIC Merge), showing basal (arrow) and apical (arrowhead) mitochondria selected for Mitotracker enrichment analysis. (Middle) Spectral fluorescence-intensity maps of Mitotracker CMXRos staining in ACs of empty vector control (L4440) and *pyk-1* RNAi treated. (Right) Quantification of relative Mitotracker CMXRos enrichment in basal mitochondria (ACs imaged and quantified during invasion at the P6.p 2–4-cell and early 4-cell stages, basal/apical; boxplot, $n \geq 5$ per condition, **** $p < 0.0001$, unpaired two-tailed t test).

Scale bars: 5 μm. See also Figure S3.

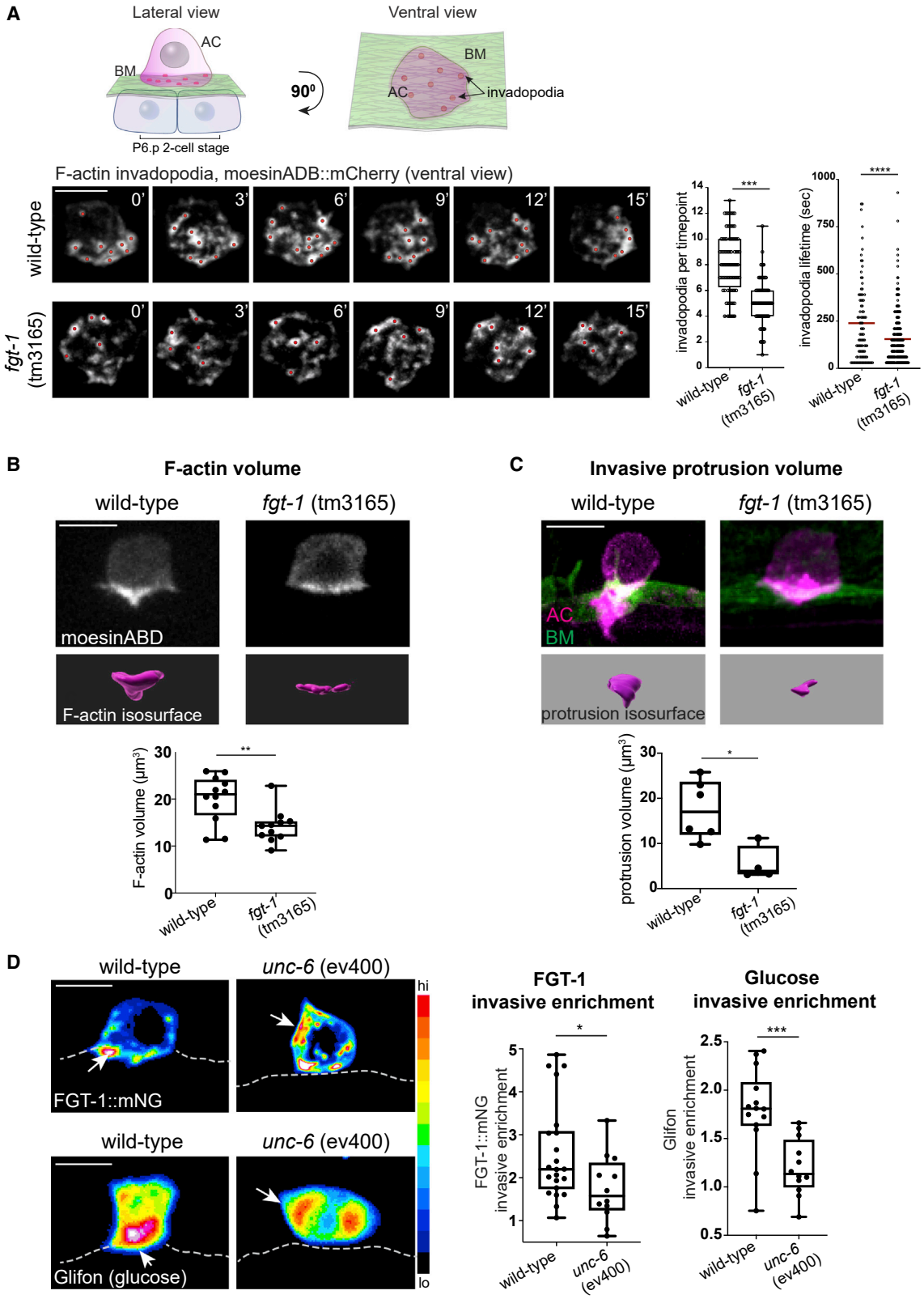

Figure 4. FGT-1 is required for invadopodia and invasive protrusion formation and is polarized by UNC-6 (netrin)

(A) (Left) Ventral view (represented by schematic, top), 3D time series of invadopodia imaged with the AC F-actin probe (*cdh-3p::mCh::moeABD*) in wild-type and *fgt-1* mutant animals at the P6.p 2-cell stage. ACs were imaged every 30 s for 15 min. Colored spots are overlaid on invadopodia as identified and tracked by

(legend continued on next page)

synapses independent of mitochondria under conditions of energy stress to support synaptic function (Jang et al., 2016). Thus, we examined whether glycolytic enzymes might concentrate near mitochondria at the AC's invasive front to support increased ATP generation. We tagged with mNG three glycolytic enzymes that function near the entry and exit points of glycolysis—phosphofructokinase (*pfk-1.1*), enolase (*enol-1a*), and pyruvate kinase (*pyk-1*) (Blanco and Blanco, 2017) (Figure 3A). Strikingly, all three glycolytic enzymes formed clusters at the invasive side of the AC and co-localized with mitochondria in the region of high ATP production. In contrast, all three glycolytic enzymes were localized diffusely in the cytosol of the ACs' apical domain (Figures 3C and S3A). The distribution of PYK-1 in neighboring noninvasive uterine cells (*ced-10p::pyk-1::mNG*) was also exclusively cytosolic (Figure S3B). We next stained mitochondria with the membrane-potential-sensitive dye Mitotracker CMXRos (Pendergrass et al., 2004) and the mitochondrial ATP reporter dye Biotracker ATP-Red 1 (Wang et al., 2016). Mitochondria at the invasive side of the AC had 2-fold greater Mitotracker CMXRos incorporation and ~1.75-fold greater ATP staining than those at the apical side (Figures S3C and S3D). Furthermore, RNAi knockdown of *pyk-1* led to invasive mitochondria no longer being enriched in Mitotracker CMXRos staining, indicating a loss of mitochondrial membrane potential and a reduced capacity to generate ATP (Figure 3D). Taken together, these results indicate that glycolytic enzymes specifically concentrate and co-localize with mitochondria at the site of invasion and enhance capacity for ATP production.

FGT-1 promotes invadopodia formation, stability, and invasive protrusion formation

The invasive protrusion machinery that breaches and removes BM is energy-intensive. Thus, we wanted to determine what aspects of BM breaching and clearance are affected by *fgt-1* loss and associated reduced ATP levels. To assess invadopodia formation and dynamics, we imaged the F-actin binding domain (ABD) of moesin (*cdh-3p*::moeABD::mCherry) and observed AC invadopodia using live-cell imaging from a ventral perspective (Figure 4A). While the size of the invadopodia in the *fgt-1* mutant were unaffected, *fgt-1* mutants had ~35% fewer invadopodia and those that formed had an ~35% shorter lifetime than wild-type animals (lifetime of ~160 versus ~240 s; Figure 4A). We next examined invasive protrusion formation in *fgt-1* mutants that breached the BM and found that while the F-actin was distributed normally at the invasive side of the AC, *fgt-1* mutant ACs had ~30% reduced F-actin volume (Figure 4B). The volume of the protrusion was also less than half of wild-type protrusions (Figures 4C and S4A). We conclude that FGT-1 is necessary for normal invadopodia formation and stability and for the generation of the large invasive protrusion that clears the opening in the BM.

UNC-6 (netrin) polarizes FGT-1 and glucose enrichment to the ACs' invasive front

UNC-6 (netrin) is secreted by the vulval P6.p cell and its descendants and orients a specialized invasive cell membrane rich in the phospholipid PI(4,5)P2 and invadopodia localized actin regulators, such as Rac GTPases and UNC-34 (ENA/Vasp) toward the BM (Hagedorn et al., 2013; Naegeli et al., 2017; Wang et al., 2014b). In *unc-6 (ev400)* mutants, PI(4,5)P2 and invadopodial actin regulators undergo dynamic clustering in all regions of the cell and no longer tightly polarize toward the BM (Wang et al., 2014a). Since FGT-1 similarly displays basal polarity in the AC, we hypothesized that FGT-1 might also be directed to the invasive membrane by UNC-6. Consistent with this idea, FGT-1 was no longer strongly localized toward the BM in *unc-6* mutant animals and was mislocalized in clusters to other regions of the cell (Figures 4D and S4B). Similarly, glucose enrichment toward the BM was lost in *unc-6* mutants, and glucose was concentrated in different regions of the AC mirroring FGT-1 mispolarization (Figure 4D). We also found that invasive enrichment of mitochondria and the associated glycolytic enzyme PFK-1.1 were disrupted in *unc-6* mutant animals. Instead, mitochondria and PFK-1.1 clusters were distributed to other regions of the AC (n = 5/6) (Figure S4C). These observations suggest that UNC-6 directs a complete invasive metabolic network—glucose transport, glucose, glycolysis, and mitochondria—to the site of BM invasion.

A synergistic screen identifies genes that function with FGT-1 to promote invasion

Complete blocks of AC invasion result in failure of the uterine-vulval connection and lead to a protruding vulva (Pvl) phenotype (Figure 5A). In *fgt-1* null mutants, Pvls rarely occur because AC invasion is delayed, but not usually blocked (Table S2; Figure S2A). The delayed invasion and reduced but still present ATP at the invasive front in *fgt-1* mutants (Figure 2G) suggested that an additional mechanism exists for importing or generating carbon sources to produce ATP for invasion. We thus conducted a synergistic interaction screen in the *fgt-1 (tm3165)* null mutant

Imaris 3D software. (Right) Quantification of the number of invadopodia per time point (boxplot) and the lifetime (in seconds) of each invadopodium (scatter plot) tracked (n = 4 animals per genotype, boxplot, *** $p < 0.001$, scatterplot, red lines indicate mean lifetime, **** $p < 0.0001$, unpaired two-tailed t tests).

(B) (Top) Maximum intensity projections of the dense F-actin network in the AC (visualized with *cdh-3p::mCherry::moeABD* at the normal time of BM breaching—P6.p 2–4-cell stage) and isosurface renderings of F-actin volume using Imaris (magenta) in wild-type and *fgt-1* mutant animals. (Bottom) Quantification of F-actin volume determined from isosurface renderings (boxplot, n = 12 per genotype, ** $p < 0.01$, unpaired two-tailed t test).

(C) (Top) Maximum intensity projections of the largest volume achieved by the invasive protrusion (magenta, visualized with *cdh-3p*::*mCherry::PLCδ^{PH}*, BM in green) during a 60-min time series. Isosurface rendering (magenta) of the volume of invasive protrusion beneath the BM. (Bottom) Quantification of invasive protrusion volume determined from isosurface renderings (ACs imaged and quantified beginning at the P.6p 2–4-cell stage, boxplot, $n \geq 4$ animals per genotype, * $p < 0.05$, unpaired two-tailed t test).

(D) (Top, left) FGT-1 (*lin-29p::fgt-1*::mNG) is polarized toward the invasive plasma membrane in the AC of a wild-type animal but is mispolarized to the apical and lateral membranes in the AC of an *unc-6* mutant animal. (Bottom, left) glucose (*lin-29p::Green Glifon 4000*) is enriched at the invasive side in the AC of a wild-type animal but is distributed in apical and lateral regions of the AC of an *unc-6* mutant animal. (Right) Quantification of invasive enrichment of FGT-1 and glucose (ACs imaged and quantified at the P6.p 2–4-cell and early 4-cell stages, boxplots, $n \geq 12$ per genotype, * $p < 0.05$, *** $p < 0.001$, unpaired two-tailed t test).

Scale bars: 5 μm. See also Figure S4.

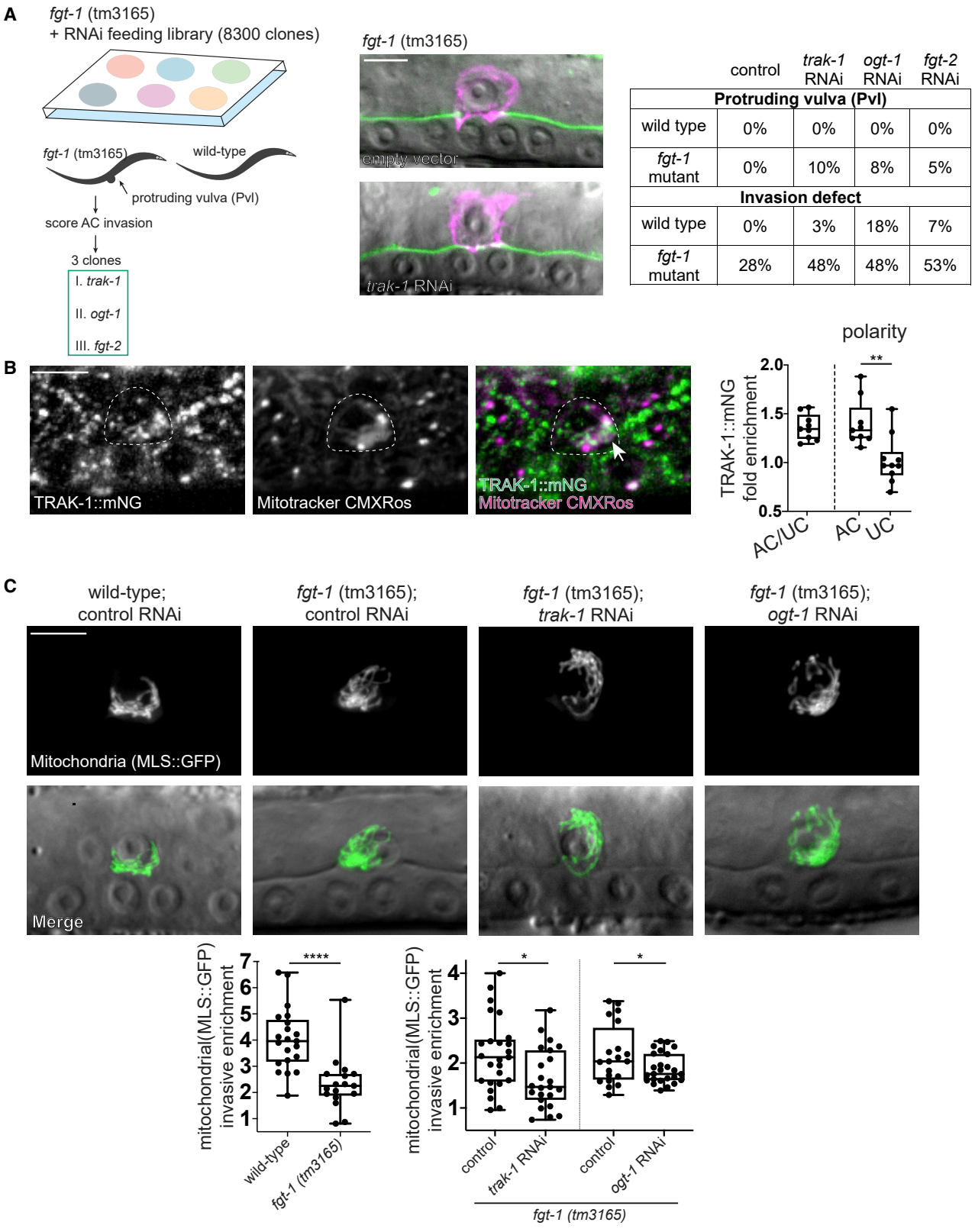

	control	*trak-1* RNAi	*ogt-1* RNAi	*fgt-2* RNAi
Protruding vulva (Pvl)				
wild type	0%	0%	0%	0%
fgt-1 mutant	0%	10%	8%	5%
Invasion defect				
wild type	0%	3%	18%	7%
fgt-1 mutant	28%	48%	48%	53%

Figure 5. TRAK-1 and OGT-1 promote mitochondrial localization to the invasive front

(A) A schematic of the synergistic interaction AC invasion screen. RNAi clones targeting ~8,300 genes were fed to newly hatched *fgt-1* mutant L1 larval stage animals. Gene knockdowns resulting in adult worms with a protruding vulval (Pvl) were scored for AC invasion defects (middle, shown at P6.p early 4-cell stage) if

(legend continued on next page)

background to identify candidate genes that act in parallel to *fgt-1* and converge on the common function of energy acquisition and ATP generation during AC invasion. We first screened for genes whose knockdown on their own did not cause a Pvl phenotype, and only did so in combination with loss of *fgt-1*. Using feeding RNAi, we targeted ~8,300 genes in *fgt-1* mutants and identified three genes that met these criteria: a mitochondrial-trafficking adaptor protein (*trak-1*), an ortholog of mammalian GLUTs (*F14E5.1*, which we have now named *fgt-2*), and an O-linked GlcNAc transferase (*ogt-1*) (Figure 5A; Table S3). We next examined whether the loss of these genes synergistically enhanced the ~30% *fgt-1* mutant AC invasion defect. While individual loss of *trak-1* and *fgt-2* via RNAi in wild-type animals (~70% and ~90% knockdown efficiency, respectively), (Figure S5D) both caused minimal invasion defects, an *ogt-1 (ok430)* null mutant displayed an ~18% invasion defect (Table S1). Notably RNAi-mediated loss of *trak-1* and *fgt-2* in the *fgt-1* mutant displayed a synergistic invasion perturbation (a defect greater than the sum of the two individual defects) (Wang and Sherwood, 2011). In contrast RNAi knockdown of *ogt-1* (~70% knockdown efficiency) (Figure S5D) in the *fgt-1* mutant was additive (Table S1). These results suggest that *ogt-1* might function in a pathway parallel to *fgt-1* to promote invasion, whereas *trak-1* and *fgt-2* act with *fgt-1* to promote carbon import and localized ATP production to fuel invasion.

TRAK-1 and OGT-1 promote mitochondrial enrichment at the invasive front

The *trak-1* gene encodes the *C. elegans* ortholog of the adaptor protein Milton/TRAK1, which links mitochondria to microtubule motor proteins for directional trafficking (Henrichs et al., 2020), and the *ogt-1* gene encodes the ortholog of O-GlcNAc transferase (OGT), which catalyzes the transfer of a sugar moiety onto nuclear and cytoplasmic proteins (Pekkurnaz et al., 2014). To understand the distribution, localization, and mitochondrial association of TRAK-1 in the AC, we endogenously tagged the *trak-1* locus (*trak-1::mNG*) and found that TRAK-1 puncta are localized in cells throughout the animal but are present at higher levels in the AC compared with neighboring uterine cells (Figure S5A). Further, TRAK-1 is enriched at ACs' invasive side but is distributed symmetrically in neighboring uterine cells (Figures 5B and S5A). Staining animals expressing TRAK-1::mNG with Mitotracker CMXRos showed that TRAK-1 co-localizes with AC mitochondria (Figure 5B). In addition, visualizing microtubules in the AC with the microtubule-binding domain of ensconsin (*lin-29p::emtb*::GFP) showed that microtubules also enrich at the ACs' invasive side (Figure S5B). Endogenous OGT-1 (*ogt-1*::GFP) (Urso et al., 2020) fluorescent signal was localized to both the nucleus and cytoplasm of the AC and uterine neighbors (Figure S5C). Given the known role of TRAK-1 and OGT-1 in regulating mitochondrial motility in neurons (Pekkurnaz et al., 2014; van Spronsen et al., 2013), we examined the role of FGT-1, TRAK-1, and OGT-1 in localizing AC mitochondria. A strain with AC mitochondria tagged with GFP (*zmp-1p::MLS::GFP*) revealed that mitochondria are concentrated more than 4-fold at the invasive side during BM breaching (Figure 5C). Surprisingly, this invasive enrichment was nearly halved in *fgt-1* mutants (Figure 5C). This suggests that glucose import and a steep intracellular glucose gradient, enhance mitochondrial positioning at the invasive front of the AC. RNAi knockdown of *trak-1* or *ogt-1* in *fgt-1* mutants further decreased mitochondrial enrichment to less than 2-fold (Figure 5C). Consistent with its synergistic genetic interaction, upon the loss of *trak-1* in *fgt-1* mutants, ACs displayed a further reduction in ATP:ADP ratio and ratio gradient compared with *fgt-1* mutants alone (Figure S5E). Notably, neither *trak-1* nor *ogt-1* RNAi alone impaired mitochondrial polarization at the ACs' invasive side (Figure S5F), indicating that TRAK-1 and OGT-1 cooperate with FGT-1 to enrich mitochondria. Together, these data indicate that FGT-1-mediated glucose import, OGT-1, and TRAK-1 are all required to position mitochondria and facilitate heightened ATP production at the invasive front to promote BM invasion.

FGT-2 cooperates with FGT-1 to import glucose for ATP production

The *fgt-2* gene (formerly *F14E5*.1) encodes a second *C. elegans* homolog of mammalian GLUTs which was previously thought to be nonfunctional based on exogenous expression in *Xenopus laevis* oocytes (Feng et al., 2013). We endogenously tagged FGT-2 (*fgt-2::mNG*), and although verified for proper insertion did not detect fluorescence in the animal, suggesting that it may be present at very low levels or is not capable of endogenous tagging. Thus, for further analyses, FGT-2 was driven by an AC-specific promoter (*cdh-3p::FGT-2::mNG*). In wild-type ACs, FGT-2 was polarized toward the invasive membrane prior to AC invasion and increased in polarity throughout invasion (Figure 6A). Notably, there was a striking rise in FGT-2 polarity right at the time of invasion (P6.p 2–4 cell stage) (Figure 6A), suggesting that FGT-2 polarization might be responsive to the increased energy needs during BM breaching. Consistent with this notion, in *fgt-1* mutants, FGT-2 enriched at the invasive membrane even more dramatically during BM breaching (Figure 6A). A greater proportion of the total FGT-2 protein within the AC was also present at the invasive membrane in *fgt-1* mutants, suggesting that

knockdown did not cause Pvls in wild-type worms. Three genes—*trak-1*, *ogt-1*, and *fgt-2* met these criteria (green box). (Right) Table shows incidence of Pvl phenotype (at early adulthood) and invasion defects (P6.p late 4-cell stage) upon knockdown of *trak-1, ogt-1* or *fgt-2* in wild-type and *fgt-1* mutant animals (Tables S1 and S3).

(B) (Left) Endogenous TRAK-1 (*trak-1::mNG*) is polarized to the invasive front (left) and co-localizes with mitochondria (middle) in the AC (circled in dotted line). Arrow in merged image indicates TRAK-1 puncta co-localized with mitochondria. (Right) Quantification showing TRAK-1 levels enriched in the AC compared with neighboring uterine cells (UC) and TRAK-1 enriched at the basal side of the AC compared with UCs (ACs imaged and quantified during invasion at the P6.p 2–4-cell and early 4-cell stages, boxplot, n = 9 animals, ** $p < 0.01$, unpaired two-tailed t test).

(C) (Top) Mitochondria (visualized with *zmp-1p::mls*::GFP) are highly enriched at the invasive side of wild-type ACs at the P6.p early 4-cell stage, and the enrichment is halved in ACs of *fgt-1* mutant animals. RNAi knockdown of *trak-1* or *ogt-1* in *fgt-1* mutants reduced AC mitochondrial enrichment further. (Bottom) Quantification of mitochondrial invasive enrichment (ACs imaged and quantified during invasion at the P6.p 2–4-cell and early 4-cell stages, boxplots, $n \geq 17$ for wt and *fgt-1* mutant conditions and $n \geq 20$ per RNAi condition, **** $p < 0.0001$, * $p < 0.05$, unpaired two-tailed t tests).

Scale bars: 5 μm. See also Figure S5.

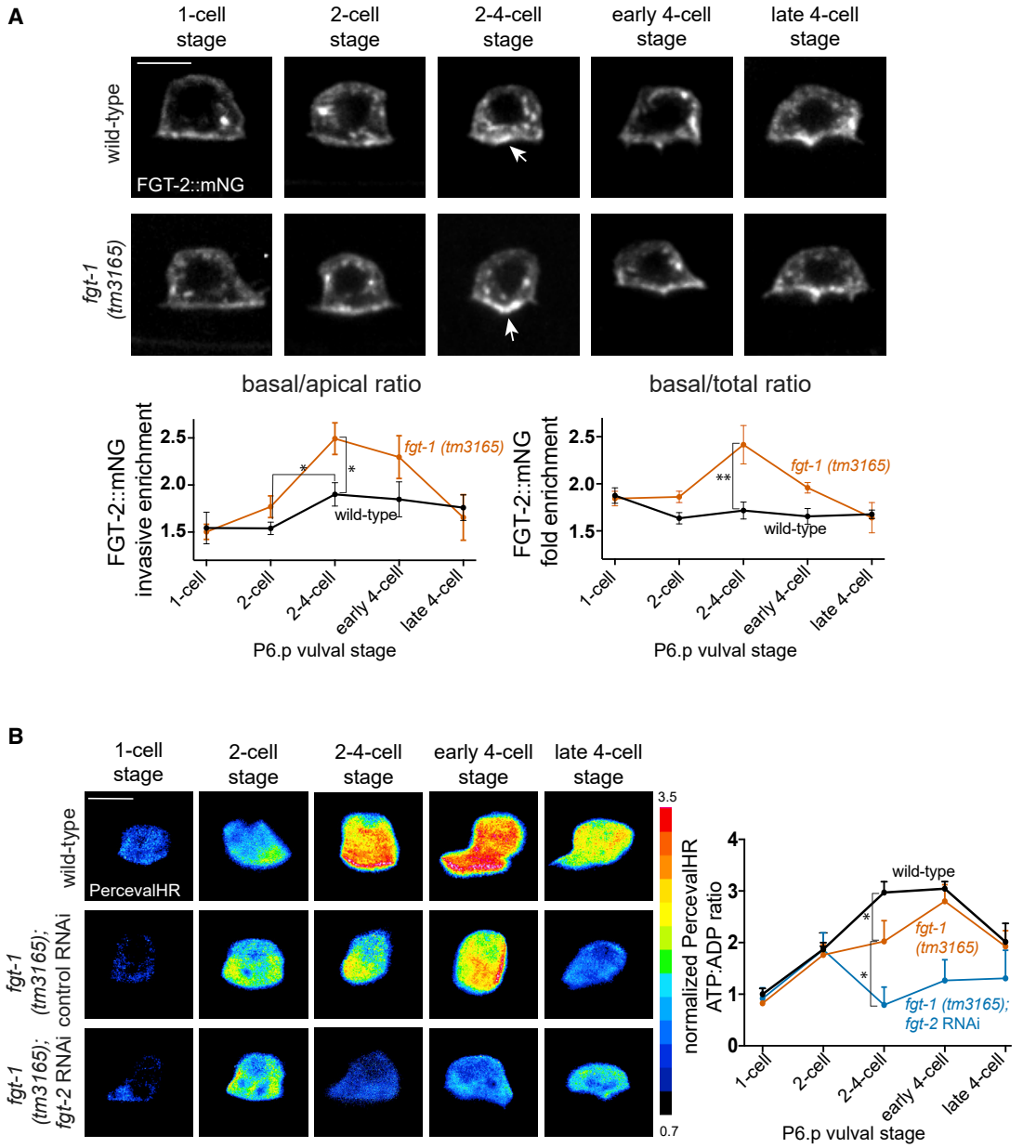

Figure 6. FGT-2 cooperates with FGT-1 to import glucose for ATP production

(A) (Top) Timeline of FGT-2 distribution in the AC (*cdh-3p::fgt-2::mNG*) shows that FGT-2 enriches at the invasive membrane at the P6.p 2–4-cell stage in wild-type animals. ACs of *fgt-1* mutant animals show greater FGT-2 invasive enrichment at the P6.p 2–4-cell stage (arrows indicate regions of enrichment). (Bottom) Quantification of invasive enrichment (basal/apical ratio) and invasive fraction of total (basal/total ratio) FGT-2 signal in wild-type (black) and *fgt-1* mutant (orange) ACs from the P6.p 1-cell to late 4-cell stages (time-course, mean ± SEM, n ≥ 5 ACs per time point, * $p < 0.025$, ** $p < 0.01$, unpaired two-tailed t tests).

(B) (Left) ATP:ADP ratio (*lin-29p*::PercevalHR) in ACs of wild-type animals, *fgt-1* mutants on empty vector RNAi (T444T), and *fgt-1* mutants on *fgt-2* RNAi before (P6.p 1-cell and 2-cell stage), during (P6.p 2–4-cell and early 4-cell stage), and after (P6.p late 4-cell stage) BM breaching; *fgt-1* mutants with *fgt-2* loss fail to generate an increase in the ATP:ADP ratio during the developmental time of BM breaching as seen in wild-type animals. (Right) Quantification of total ATP:ADP ratio in ACs of wild-type (black), *fgt-1* mutants (orange), and *fgt-1* mutants on *fgt-2* RNAi (blue) over developmental time (n ≥ 4 ACs per time point, mean ± SEM, * $p < 0.05$, one-way ANOVA with *post hoc* Tukey's test).

Scale bars: 5 μm. See also Figure S6.

more FGT-2 within the cells endomembrane system is trafficked to the invasive membrane (Figure 6A). In contrast, FGT-1 enrichment to the invasive membrane was not increased by *fgt-2* knockdown (Figure S6A).

To further test whether FGT-2 could be adaptively responsive to the metabolic needs of BM breaching, we examined the localization of FGT-2 in the ACs of animals that were genetically null for five matrix metalloproteinases (MMP-animals) that are

expressed either in the AC or neighboring tissues at the time of invasion (Kelley et al., 2019). We have previously shown that in MMP-animals, ACs adaptively polymerize more F-actin to breach the BM with physical force and that this adaptation is supported by increased mitochondrial enrichment at the invasive front. Consistent with an adaptive role for FGT-2 in supplying increased glucose during invasion, FGT-2 was more enriched at the AC's invasive plasma membrane in MMP-animals and a greater proportion of total FGT-2 in the AC was present at the invasive plasma membrane (Figure S6C).

Finally, we examined how *fgt-2* loss affects glucose import and ATP production in the *fgt-1* mutant. RNAi-mediated knockdown of *fgt-2* in *fgt-1* null mutants further reduced glucose enrichment at the invasive front (Figure S6B). Examination of the ATP:ADP ratio during the entire period of invasion revealed that, in *fgt-1* mutants alone, the peak increase in the ATP:ADP ratio was delayed, which is consistent with the delay in invasion and the apparent compensatory increased enrichment of FGT-2 at the invasive membrane (Figure 6B). Notably, RNAi-mediated reduction of *fgt-2* in *fgt-1* mutant animals eliminated the burst of ATP during the time of BM breaching (Figure 6B). We conclude that FGT-2 works in concert with FGT-1 to adaptively tune glucose import and fuel rapid ATP production to breach the BM during AC invasion.

DISCUSSION

Extensive studies have revealed the F-actin regulators, membrane-trafficking mechanisms, and signaling inputs that generate invasive protrusions that breach BM barriers (Di Martino et al., 2016; Eddy et al., 2017; Hastie and Sherwood, 2016; Masi et al., 2020). In contrast, little is known about how invasive cells metabolically support these energy-consuming cellular structures. By expressing the PercevalHR biosensor in the AC (Tantama et al., 2013), we found that the ATP:ADP ratio increased dramatically during the time of BM breaching and that this increase was driven by ATP production. Recent metabolic profiling and pharmacological inhibition studies have indicated that mitochondrial OXPHOS promotes invasiveness in a number of cancers, such as melanoma (Salhi et al., 2020), breast (Wu et al., 2021), ovarian (Sun et al., 2017), prostate (Rivadeneira et al., 2015), and pancreatic (Papalazarou et al., 2020). Consistent with a role for mitochondrial OXPHOS in supporting invasion, mitochondria localize to invasive protrusions of metastatic ovarian cancer and melanoma cells during invasion through dense collagen gels (Cunniff et al., 2016). Our work also indicates that a reliance on OXPHOS during a developmental invasion event—as we found that mitochondria enrich at the AC's invasive front where the highest ATP levels are concentrated—and the impairment of OXPHOS with rotenone, an inhibitor of ETC Complex I, markedly decreased ATP levels and inhibited invasion. Our findings that ATP levels increased dramatically during BM crossing also add to growing evidence that invasive cells must provide high levels of ATP to meet the energy demands of transmigrating dense ECMs. For example, the ATP:ADP ratio of breast cancer cells increases when migrating through compact collagen matrices (Wu et al., 2021; Zanotelli et al., 2018) and pancreatic ductal carcinoma cells produce more ATP when cultured in Matrigel, a reconstituted BM-derived matrix (Papalazarou et al., 2020).

Localized mitochondria and ATP production are not unique to invasive cells. Mitochondria also localize near energy-demanding contractile muscle myofibrils (Glancy et al., 2015) and at neuronal synapses, growth cones, and dendrites (Devine and Kittler, 2018; Rangaraju et al., 2019; Smith and Gallo, 2018). Understanding how cells acquire nutrients to fuel localized mitochondria has been stymied by numerous nutrient transporters and flexible nutrient storage and uptake mechanisms (Palm and Thompson, 2017). By conducting a targeted AC-specific RNAi screen and an unbiased synthetic interaction screen, we identified two facilitated GLUTs, FGT-1 and FGT-2, which cooperate to import glucose into the AC during BM breaching. Both FGT-1 and FGT-2 polarized along the AC's invasive cell membrane prior to BM breaching. Notably, FGT-2 enrichment at the invasive membrane increased specifically during BM breaching, and in the absence of FGT-1, FGT-2 became even more concentrated at the invasive membrane by shifting out of a cytoplasmic pool. In contrast, FGT-1 polarization did not increase upon loss of FGT-2. This suggests that FGT-1 and FGT-2 form a robust and adaptable glucose-import system that can tune glucose import to meet increased energy demands during BM breaching. Consistent with the localization of FGT-1 and FGT-2, a glucose biosensor revealed an intracellular gradient of glucose originating at the invasive plasma membrane that is dependent on FGT-1 and FGT-2. Our evidence suggests that glucose import near the invasive front mitochondria is required to generate high levels of ATP during invasion, as the loss of FGT-1 together with reduction of FGT-2 eliminated the ATP burst. Local import might be required because glucose diffusion within cells is limited by the structured cytoplasmic environment (Kreft et al., 2013). Adaptable glucose import may support invasion in many contexts. For example, *in vitro* selection for super invasive human cervix squamous cell carcinoma cells identified cells with increased invasive ability that also gained enhanced glucose uptake (Porporato et al., 2014). In addition, visualization of the fluorescent glucose analog 2-NBDG has revealed that both individually invading breast cancer cells, as well as leader cells of collectively invading groups, increase their glucose uptake in dense collagen matrices (Zanotelli et al., 2018; Zhang et al., 2019). Thus, tunable local glucose uptake might be a common strategy to fuel the highly localized and changing needs of invasive cells.

Glucose must be converted into pyruvate to allow its breakdown within mitochondria to produce ATP via OXPHOS (Wilson, 2017). Glycolysis involves the sequential action of ten enzymes that convert glucose into two molecules of pyruvate. There is growing evidence that diverse formations and subcellular localizations of glycolytic enzymes help channel substrates between enzymes to meet cellular and subcellular needs for glycolytic output: ATP, pyruvate, and possibly nucleotide biosynthesis metabolites (Jang et al., 2021; Kohnhorst et al., 2017). For example, mitochondria-independent condensates of glycolytic enzymes form adjacent to synapses in *C. elegans* neurons during energy stress to support synaptic function (Jang et al., 2016). In addition, during hypoxia, yeast glycolytic enzymes coalesce in a phase-separated G-body compartment, which promotes glucose consumption and cell survival (Jin et al., 2017).

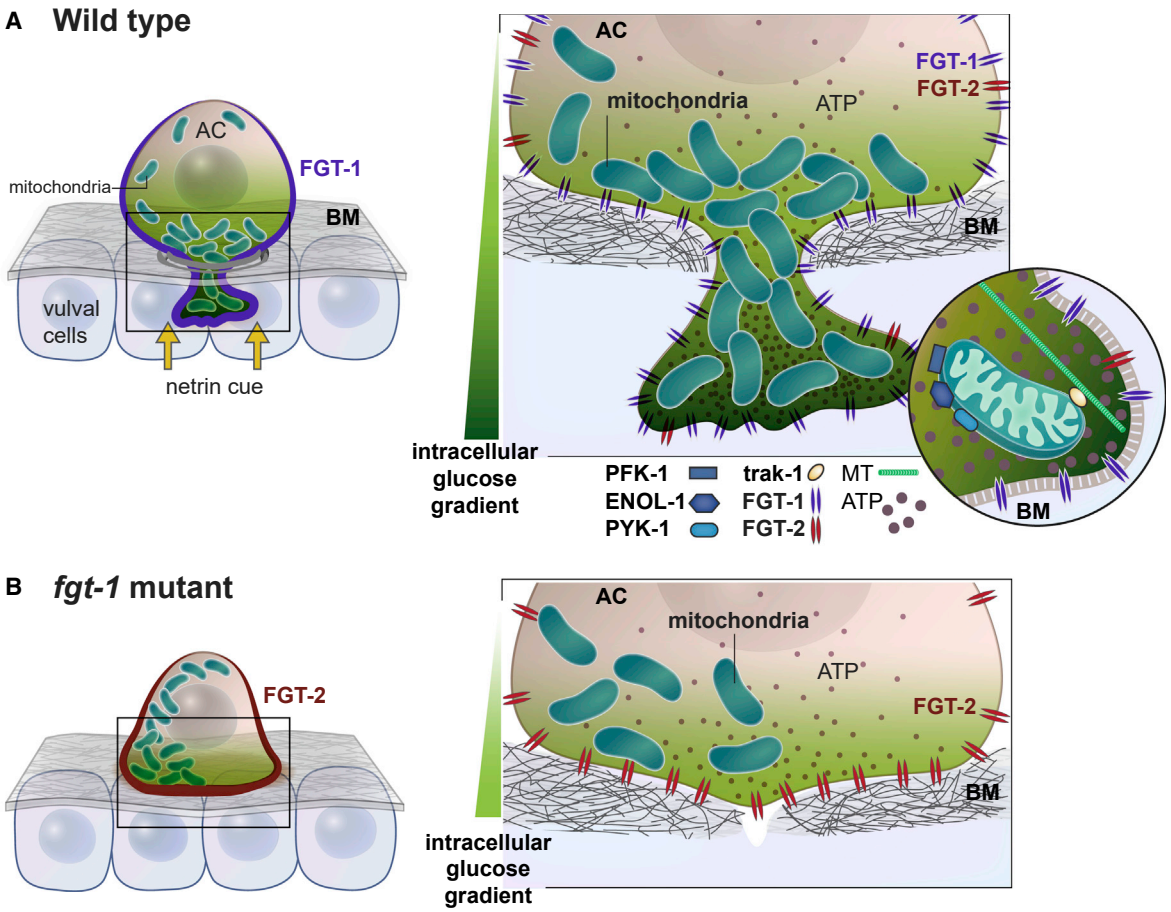

Figure 7. A localized, integrated, and adaptive metabolic network fuels AC-BM invasion

(A) The glucose transporter FGT-1 is enriched at the invasive plasma membrane of wild-type ACs in response to the UNC-6 (netrin) invasive polarity cue and sets up an intracellular glucose gradient. FGT-2 is also localized to a lesser extent. Mitochondria concentrate to the invasive side of the AC in part via the glucose-dependent activity of TRAK-1 and OGT-1 (OGT-1 not shown). Glycolytic enzymes cluster and co-localize specifically with invasive front mitochondria. Together, high levels of local glucose, local glycolytic breakdown to pyruvate, and elevated mitochondria numbers, produce high levels of ATP at the invasive front to power the protrusive cellular machinery for BM breaching.

(B) In the absence of FGT-1, more FGT-2 localizes to the AC's invasive cell membrane, revealing adaptive properties. However, AC glucose levels are still lower than wild-type animals, and mitochondria fail to localize correctly to the invasive side and less ATP is produced at the invasive front, thus delaying invasion through the BM.

Glycolytic enzymes also concentrate along erythrocyte membranes for ATP production where they support channel activity and signaling (Campanella et al., 2005, 2008). By fluorescently tagging and examining the localization of three glycolytic enzymes near the entry and at the exit points of glycolysis—phosphofructokinase (PFK-1), enolase (ENOL-1), and pyruvate kinase (PYK-1)—we discovered that all three formed clusters that co-localize with the ACs' invasive front mitochondria. Staining with the membrane potential-sensitive dye Mitotracker CMXRos and the mitochondrial ATP dye BioTracker ATP-Red 1 indicated that these invasive mitochondria have greater ATP production capacity and ATP output, which is lost after impairing glycolysis. Notably, biochemical analyses and enzyme-activity assays have shown that all glycolytic enzymes associate with mitochondria in *Arabidopsis thaliana* (Giegé et al., 2003; Graham et al., 2007) and *Saccharomyces cerevisiae* (Brandina et al., 2006). Respiration and metabolite analysis have suggested mitochondrial associated glycolytic enzymes facilitate rapid channeling of substrates between enzymes to more efficiently convert glucose to pyruvate and support mitochondrial OXPHOS (Graham et al., 2007). Our observations are consistent with a similar but spatially restricted system that rapidly converts the high levels of imported glucose at the invasive front into pyruvate to generate highly active mitochondria that supply ATP to fuel the AC's invasive machinery. It will be important to determine if mitochondria localized to the leading edge of other migratory and invasive cancer cells and fibroblasts, as well as in neurons in energy-demanding synapses, growth cones, and dendrites also associate with glycolytic enzymes, as this might be a shared means to provide a robust fuel source for highly active mitochondria.

Invadopodia and large protrusions that breach and clear BM barriers require energy-demanding F-actin turnover and membrane trafficking (Li et al., 2019; Marshansky and Futai, 2008;

Shah et al., 2015). We found that FGT-1-mediated glucose import supports the formation and stability of invadopodia and the generation of the invasive protrusion that clears the BM. Our work also revealed that the invasive machinery and the metabolic components that fuel it are interlinked. We previously showed that UNC-6 (netrin) secreted from the central vulval cells polarizes the specialized invasive cell membrane rich in the phospholipid PI(4,5)P2, the lysosomal membrane store that contributes to the invasive protrusion, and numerous actin regulators that form the invasive machinery, toward the BM (Naegeli et al., 2017; Wang et al., 2014b; Ziel et al., 2009). We discovered here that UNC-6 also polarizes FGT-1 to the invasive membrane, which generates a glucose gradient emanating from the invasive side of the AC. Our work suggests that this glucose gradient not only provides a fuel source for mitochondria, but also helps localize mitochondria, as loss of FGT-1 decreased mitochondrial enrichment at the invasive front. Studies in cultured neurons have found that high levels of extracellular glucose arrest mitochondrial movement via the activity of the enzyme OGT, which diminishes mitochondrial motility by modifying the mitochondrial adaptor protein TRAK1 (Pekkurnaz et al., 2014). Strikingly, our genome-scale synergistic screen identified *ogt-1* and *trak-1* as enhancing the *fgt*-1 invasion defect. Our genetic and cell biological studies indicate that these genes act together to localize mitochondria at the invasive front of the AC, as TRAK-1 co-localizes with mitochondria near the site of invasion and reduction of *ogt-1* or *trak-1* in *fgt-1* mutants led to a further loss of invasive mitochondrial enrichment. Further, locally imported glucose via FGT-1 and FGT-2 might also serve as the source of a substrate for OGT-1 enzymatic activity at the site of invasion. Together, our findings reveal a robust, adaptable, and high-capacity metabolic network in the AC that is an integrated component of the specialized invasive program (Figure 7). This metabolic network facilitates local and dynamic ATP production to fuel the specialized invasive protrusions that breach and clear BM barriers. We expect that similar metabolic networks might fuel matrix breaching in other invasive cells and may provide new therapeutic strategies in human diseases such as cancer, where unchecked invasive behavior underlies metastasis and disease progression.

Limitations of the study

Our study used an RNAi-knockdown-based screen to identify synthetic genetic interactions with *fgt-1* during invasion and found three candidate genes that interact with FGT-1 mediated glucose import to promote cell invasion. Due to the inherent limitations of RNAi-based knockdown, we might have failed to identify other synthetic interactions due to the lack of full *C. elegans* gene representation in the RNAi library, insufficient RNAi knockdown, functional redundancy with another ortholog, or interactions producing mild invasion defects that would not result in a plate-level Pvl phenotype. Finally, while we show that FGT-2 can adaptively tune glucose import in the absence of FGT-1 or MMPs, how the AC detects an increased requirement for glucose, and the mechanisms by which FGT-2 is trafficked to the cell surface to meet this adaptive need were not determined in this study. Future work to address this adaptive mechanism could explore the mechanosensing and energy-sensing pathways in the AC during BM breaching.

STAR★METHODS

Detailed methods are provided in the online version of this paper and include the following:

- KEY RESOURCES TABLE
- RESOURCE AVAILABILITY
  - Lead contact
  - Materials availability
  - Data and code availability
- EXPERIMENTAL MODEL AND SUBJECT DETAILS
- METHOD DETAILS
  - Construction of transgenic strains
  - Construction of Genome-edited Strains
  - Feeding RNAi
  - Microscopy and image acquisition
  - Stimulated Raman scattering (SRS) microscopy
  - Imaging PercevalHR
  - Imaging Rosella
  - Imaging Green Glifon 4000
  - 2-deoxyglucose, Phloretin and Rotenone Treatment
  - Staining with Mitochondrial Dyes
- QUANTIFICATION AND STATISTICAL ANALYSIS
  - Analysis of Metabolic Biosensors
  - Analysis of fluorescence enrichment in the AC and Invasive Membrane
  - Mitotracker CMXRos Invasive Mitochondrial Enrichment
  - Colocalization analysis
  - Invadopodia dynamics, F-actin volume, and Protrusion expansion
  - RNAi knockdown efficiency
  - Spectral representation of fluorescence intensity
  - Statistical analyses

SUPPLEMENTAL INFORMATION

Supplemental information can be found online at https://doi.org/10.1016/j.devcel.2022.02.019.

ACKNOWLEDGMENTS

We thank Lisa Cameron of the Duke University LMCF for imaging advice and E. Hastie, R. Jayadev, and C. Gianakas for comments on the manuscript. We thank A. Kawska (info@illuscientia) for her work on schematics. We thank the Colón-Ramos lab for supplying plasmids with glycolytic enzyme coding sequences and Calico Life Sciences for supplying the plasmid encoding PercevalHR. A.G., I.W.K., L.C.K., Q.C., and D.R.S. are supported by R35GM118049-06. A.S.M. and M.C.W. are supported by NIH grants (R01AG045183, R01AT009050, and DP1DK113644), March of Dimes Foundation, Welch Foundation, and the Howard Hughes Medical Institute. Some strains were provided by the Caenorhabditis Genetics Center, which is funded by National Institutes of Health Office of Research Infrastructure Programs (P40 OD010440).

AUTHOR CONTRIBUTIONS

Conceptualization: A.G. and D.R.S.; methodology: A.G., I.W.K., L.C.K., Q.C., A.S.M., M.C.W., and D.R.S.; formal analysis: A.G.; investigation: A.G., I.W.K., L.C.K., Q.C., and A.S.M.; writing—original draft: A.G. and D.R.S.; writing—review and editing: A.G., A.S.M., M.C.W., and D.R.S.; visualization: A.G.; funding acquisition: M.C.W. and D.R.S.; resources: D.R.S.; supervision, D.R.S.

DECLARATION OF INTERESTS

The authors declare no competing interests.

Received: October 5, 2021
Revised: January 18, 2022
Accepted: February 18, 2022
Published: March 21, 2022

REFERENCES

Al-Rekabi, Z., Cunningham, M.L., and Sniadecki, N.J. (2017). Cell mechanics of craniosynostosis. ACS Biomater. Sci. Eng. *3*, 2733–2743.

Blanco, A., and Blanco, G. (2017). Carbohydrate metabolism. In Medical Biochemistry (Elsevier), pp. 283–323.

Bohnert, K.A., and Kenyon, C. (2017). A lysosomal switch triggers proteostasis renewal in the immortal *C. elegans* germ lineage. Nature *551*, 629–633.

Bonora, M., Patergnani, S., Rimessi, A., De Marchi, E., Suski, J.M., Bononi, A., Giorgi, C., Marchi, S., Missiroli, S., Poletti, F., et al. (2012). ATP synthesis and storage. Purinergic Signal. *8*, 343–357.

Brandina, I., Graham, J., Lemaitre-Guillier, C., Entelis, N., Krasheninnikov, I., Sweetlove, L., Tarassov, I., and Martin, R.P. (2006). Enolase takes part in a macromolecular complex associated to mitochondria in yeast. Biochim. Biophys. Acta *1757*, 1217–1228.

Brenner, S. (1974). The genetics of *Caenorhabditis elegans*. Genetics *77*, 71–94.

Bricker, D.K., Taylor, E.B., Schell, J.C., Orsak, T., Boutron, A., Chen, Y.-C., Cox, J.E., Cardon, C.M., Van Vranken, J.G., Dephoure, N., et al. (2012). A mitochondrial pyruvate carrier required for pyruvate uptake in yeast, *Drosophila*, and humans. Science *337*, 96–100.

Caino, M.C., Ghosh, J.C., Chae, Y.C., Vaira, V., Rivadeneira, D.B., Faversani, A., Rampini, P., Kossenkov, A.V., Aird, K.M., Zhang, R., et al. (2015). PI3K therapy reprograms mitochondrial trafficking to fuel tumor cell invasion. Proc. Natl. Acad. Sci. USA *112*, 8638–8643.

Cambi, A., and Chavrier, P. (2021). Tissue remodeling by invadosomes. Fac. Rev. *10*, 39.

Campanella, M.E., Chu, H., and Low, P.S. (2005). Assembly and regulation of a glycolytic enzyme complex on the human erythrocyte membrane. Proc. Natl. Acad. Sci. USA *102*, 2402–2407.

Campanella, M.E., Chu, H., Wandersee, N.J., Peters, L.L., Mohandas, N., Gilligan, D.M., and Low, P.S. (2008). Characterization of glycolytic enzyme interactions with murine erythrocyte membranes in wild-type and membrane protein knockout mice. Blood *112*, 3900–3906.

Chan, Z.C.-K., Kwan, H.-L.R., Wong, Y.S., Jiang, Z., Zhou, Z., Tam, K.W., Chan, Y.-S., Chan, C.B., and Lee, C.W. (2020). Site-directed MT1-MMP trafficking and surface insertion regulate AChR clustering and remodeling at developing NMJs. eLife *9*, e54379.

Chen, X., Qian, Y., and Wu, S. (2015). The Warburg effect: evolving interpretations of an established concept. Free Radic. Biol. Med. *79*, 253–263.

Chen, Y.-C., Baik, M., Byers, J.T., Chen, K.T., French, S.W., and Díaz, B. (2019). TKS5-positive invadopodia-like structures in human tumor surgical specimens. Exp. Mol. Pathol. *106*, 17–26.

Cunniff, B., McKenzie, A.J., Heintz, N.H., and Howe, A.K. (2016). AMPK activity regulates trafficking of mitochondria to the leading edge during cell migration and matrix invasion. Mol. Biol. Cell *27*, 2662–2674.

Devine, M.J., and Kittler, J.T. (2018). Mitochondria at the neuronal presynapse in health and disease. Nat. Rev. Neurosci. *19*, 63–80.

Di Martino, J., Henriet, E., Ezzoukhry, Z., Goetz, J.G., Moreau, V., and Saltel, F. (2016). The microenvironment controls invadosome plasticity. J. Cell Sci. *129*, 1759–1768.

Dickinson, D.J., and Goldstein, B. (2016). CRISPR-based methods for *Caenorhabditis elegans* genome engineering. Genetics *202*, 885–901.

Eddy, R.J., Weidmann, M.D., Sharma, V.P., and Condeelis, J.S. (2017). Tumor cell invadopodia: invasive protrusions that orchestrate metastasis. Trends Cell Biol. *27*, 595–607.

Edelstein, A.D., Tsuchida, M.A., Amodaj, N., Pinkard, H., Vale, R.D., and Stuurman, N. (2014). Advanced methods of microscope control using μManager software. J Biol Methods *1*, e10. https://doi.org/10.14440/jbm.2014.36.

Ezzoukhry, Z., Henriet, E., Cordelières, F.P., Dupuy, J.-W., Maître, M., Gay, N., Di-Tommaso, S., Mercier, L., Goetz, J.G., Peter, M., et al. (2018). Combining laser capture microdissection and proteomics reveals an active translation machinery controlling invadosome formation. Nat. Commun. *9*, 2031.

Faul, F., Erdfelder, E., Lang, A.G., and Buchner, A. (2007). G*Power 3: A flexible statistical power analysis program for the social, behavioral, and biomedical sciences. Behav Res Methods *39*, 175–191.

Feng, Y., Williams, B.G., Koumanov, F., Wolstenholme, A.J., and Holman, G.D. (2013). FGT-1 is the major glucose transporter in *C. elegans* and is central to aging pathways. Biochem. J. *456*, 219–229.

Fisher, S.J. (2015). Why is placentation abnormal in preeclampsia? Am. J. Obstet. Gynecol. *213*, S115–S122.

Garde, A., and Sherwood, D.R. (2021). Fueling cell invasion through extracellular matrix. Trends Cell Biol. *31*, 445–456.

Giegé, P., Heazlewood, J.L., Roessner-Tunali, U., Millar, A.H., Fernie, A.R., Leaver, C.J., and Sweetlove, L.J. (2003). Enzymes of glycolysis are functionally associated with the mitochondrion in *Arabidopsis* cells. Plant Cell *15*, 2140–2151.

Glancy, B., Hartnell, L.M., Malide, D., Yu, Z.-X., Combs, C.A., Connelly, P.S., Subramaniam, S., and Balaban, R.S. (2015). Mitochondrial reticulum for cellular energy distribution in muscle. Nature *523*, 617–620.

Graham, J.W.A., Williams, T.C.R., Morgan, M., Fernie, A.R., Ratcliffe, R.G., and Sweetlove, L.J. (2007). Glycolytic enzymes associate dynamically with mitochondria in response to respiratory demand and support substrate channeling. Plant Cell *19*, 3723–3738.

Hagedorn, E.J., Kelley, L.C., Naegeli, K.M., Wang, Z., Chi, Q., and Sherwood, D.R. (2014). ADF/cofilin promotes invadopodial membrane recycling during cell invasion in vivo. J. Cell Biol. *204*, 1209–1218.

Hagedorn, E.J., Yashiro, H., Ziel, J.W., Ihara, S., Wang, Z., and Sherwood, D.R. (2009). Integrin acts upstream of netrin signaling to regulate formation of the anchor cell's invasive membrane in *C. elegans*. Dev. Cell *17*, 187–198.

Hagedorn, E.J., Ziel, J.W., Morrissey, M.A., Linden, L.M., Wang, Z., Chi, Q., Johnson, S.A., and Sherwood, D.R. (2013). The netrin receptor DCC focuses invadopodia-driven basement membrane transmigration in vivo. J. Cell Biol. *201*, 903–913.

Hastie, E.L., and Sherwood, D.R. (2016). A new front in cell invasion: the invadopodial membrane. Eur. J. Cell Biol. *95*, 441–448.

Henrichs, V., Grycova, L., Barinka, C., Nahacka, Z., Neuzil, J., Diez, S., Rohlena, J., Braun, M., and Lansky, Z. (2020). Mitochondria-adaptor TRAK1 promotes kinesin-1 driven transport in crowded environments. Nat. Commun. *11*, 3123.

Herzig, S., Raemy, E., Montessuit, S., Veuthey, J.-L., Zamboni, N., Westermann, B., Kunji, E.R.S., and Martinou, J.-C. (2012). Identification and functional expression of the mitochondrial pyruvate carrier. Science *337*, 93–96.

Jang, S., Nelson, J.C., Bend, E.G., Rodríguez-Laureano, L., Tueros, F.G., Cartagenova, L., Underwood, K., Jorgensen, E.M., and Colón-Ramos, D.A. (2016). Glycolytic enzymes localize to synapses under energy stress to support synaptic function. Neuron *90*, 278–291.

Jang, S., Xuan, Z., Lagoy, R.C., Jawerth, L.M., Gonzalez, I.J., Singh, M., Prashad, S., Kim, H.S., Patel, A., Albrecht, D.R., et al. (2021). Phosphofructokinase relocalizes into subcellular compartments with liquid-like properties in vivo. Biophys. J. *120*, 1170–1186.

Jayadev, R., and Sherwood, D.R. (2017). Basement membranes. Curr. Biol. *27*, R207–R211.

Jin, M., Fuller, G.G., Han, T., Yao, Y., Alessi, A.F., Freeberg, M.A., Roach, N.P., Moresco, J.J., Karnovsky, A., Baba, M., et al. (2017). Glycolytic enzymes coalesce in G bodies under hypoxic stress. Cell Rep. *20*, 895–908.

Kamath, R.S., and Ahringer, J. (2003). Genome-wide RNAi screening in *Caenorhabditis elegans*. Methods *30*, 313–321.

Keeley, D.P., Hastie, E., Jayadev, R., Kelley, L.C., Chi, Q., Payne, S.G., Jeger, J.L., Hoffman, B.D., and Sherwood, D.R. (2020). Comprehensive endogenous tagging of basement membrane components reveals dynamic movement within the matrix scaffolding. Dev. Cell *54*, 60–74.e7.

Kelley, L.C., Chi, Q., Cáceres, R., Hastie, E., Schindler, A.J., Jiang, Y., Matus, D.Q., Plastino, J., and Sherwood, D.R. (2019). Adaptive F-actin polymerization and localized ATP production drive basement membrane invasion in the absence of MMPs. Dev. Cell *48*, 313–328.e8.

Kelley, L.C., Lohmer, L.L., Hagedorn, E.J., and Sherwood, D.R. (2014). Traversing the basement membrane in vivo: a diversity of strategies. J. Cell Biol. *204*, 291–302.

Kelley, L.C., Wang, Z., Hagedorn, E.J., Wang, L., Shen, W., Lei, S., Johnson, S.A., and Sherwood, D.R. (2017). Live-cell confocal microscopy and quantitative 4D image analysis of anchor-cell invasion through the basement membrane in *Caenorhabditis elegans*. Nat. Protoc. *12*, 2081–2096.

Kitaoka, S., Morielli, A.D., and Zhao, F.-Q. (2013). FGT-1 is a mammalian GLUT2-like facilitative glucose transporter in *Caenorhabditis elegans* whose malfunction induces fat accumulation in intestinal cells. PLoS One *8*, e68475.

Kohnhorst, C.L., Kyoung, M., Jeon, M., Schmitt, D.L., Kennedy, E.L., Ramirez, J., Bracey, S.M., Luu, B.T., Russell, S.J., and An, S. (2017). Identification of a multienzyme complex for glucose metabolism in living cells. J. Biol. Chem. *292*, 9191–9203.

Kreft, M., Lukšič, M., Zorec, T.M., Prebil, M., and Zorec, R. (2013). Diffusion of D-glucose measured in the cytosol of a single astrocyte. Cell. Mol. Life Sci. *70*, 1483–1492.

Leonard, C.E., and Taneyhill, L.A. (2020). The road best traveled: neural crest migration upon the extracellular matrix. Semin. Cell Dev. Biol. *100*, 177–185.

Li, Y., Yao, L., Mori, Y., and Sun, S.X. (2019). On the energy efficiency of cell migration in diverse physical environments. Proc. Natl. Acad. Sci. USA *116*, 23894–23900.

Marshansky, V., and Futai, M. (2008). The V-type H+-ATPase in vesicular trafficking: targeting, regulation and function. Curr. Opin. Cell Biol. *20*, 415–426.

Masi, I., Caprara, V., Bagnato, A., and Rosanò, L. (2020). Tumor cellular and microenvironmental cues controlling invadopodia formation. Front. Cell Dev. Biol. *8*, 584181.

Mita, M., Ito, M., Harada, K., Sugawara, I., Ueda, H., Tsuboi, T., and Kitaguchi, T. (2019). Green fluorescent protein-based glucose indicators report glucose dynamics in living cells. Anal. Chem. *91*, 4821–4830.

Morrissey, M.A., Keeley, D.P., Hagedorn, E.J., McClatchey, S.T.H., Chi, Q., Hall, D.H., and Sherwood, D.R. (2014). B-LINK: a hemicentin, plakin, and integrin-dependent adhesion system that links tissues by connecting adjacent basement membranes. Dev. Cell *31*, 319–331.

Moser, G., Windsperger, K., Pollheimer, J., de Sousa Lopes, S.C., and Huppertz, B. (2018). Human trophoblast invasion: new and unexpected routes and functions. Histochem. Cell Biol. *150*, 361–370.

Mutlu, A.S., Chen, T., Deng, D., and Wang, M.C. (2021). Label-free imaging of lipid storage dynamics in *Caenorhabditis elegans* using stimulated Raman scattering microscopy. J. Vis. Exp. *171*, e61870.

Naegeli, K.M., Hastie, E., Garde, A., Wang, Z., Keeley, D.P., Gordon, K.L., Pani, A.M., Kelley, L.C., Morrissey, M.A., Chi, Q., et al. (2017). Cell invasion in vivo via rapid exocytosis of a transient lysosome-derived membrane domain. Dev. Cell *43*, 403–417.e10.

Nichols, E.L., and Smith, C.J. (2019). Pioneer axons employ Cajal's battering ram to enter the spinal cord. Nat. Commun. *10*, 562.

Palm, W., and Thompson, C.B. (2017). Nutrient acquisition strategies of mammalian cells. Nature *546*, 234–242.

Papalazarou, V., Zhang, T., Paul, N.R., Juin, A., Cantini, M., Maddocks, O.D.K., Salmeron-Sanchez, M., and Machesky, L.M. (2020). The creatine-phosphagen system is mechanoresponsive in pancreatic adenocarcinoma and fuels invasion and metastasis. Nat. Metab. *2*, 62–80.

Paterson, E.K., and Courtneidge, S.A. (2018). Invadosomes are coming new insights into function and disease relevance. FEBS J. *285*, 8–27.

Pekkurnaz, G., Trinidad, J.C., Wang, X., Kong, D., and Schwarz, T.L. (2014). Glucose regulates mitochondrial motility via Milton modification by O-GlcNAc transferase. Cell *158*, 54–68.

Pendergrass, W., Wolf, N., and Poot, M. (2004). Efficacy of MitoTracker Green and CMXrosamine to measure changes in mitochondrial membrane potentials in living cells and tissues. Cytometry A *61*, 162–169.

Porporato, P.E., Payen, V.L., Pérez-Escuredo, J., De Saedeleer, C.J., Danhier, P., Copetti, T., Dhup, S., Tardy, M., Vazeille, T., Bouzin, C., et al. (2014). A mitochondrial switch promotes tumor metastasis. Cell Rep. *8*, 754–766.

Pozzi, A., Yurchenco, P.D., and Iozzo, R.V. (2017). The nature and biology of basement membranes. Matrix Biol. *57–58*, 1–11.

Rambold, A.S., Cohen, S., and Lippincott-Schwartz, J. (2015). Fatty acid trafficking in starved cells: regulation by lipid droplet lipolysis, autophagy, and mitochondrial fusion dynamics. Dev. Cell *32*, 678–692.

Rangaraju, V., Lauterbach, M., and Schuman, E.M. (2019). Spatially stable mitochondrial compartments fuel local translation during plasticity. Cell *176*, 73–84.e15.

Reuten, R., Zendehroud, S., Nicolau, M., Fleischhauer, L., Laitala, A., Kiderlen, S., Nikodemus, D., Wullkopf, L., Nielsen, S.R., McNeilly, S., et al. (2021). Basement membrane stiffness determines metastases formation. Nat. Mater. *20*, 892–903.

Richardson, C.E., Spilker, K.A., Cueva, J.A., Perrino, J., Goodman, M.B., and Shen, K. (2014). PTRN-1, a microtubule minus end-binding CAMSAP homolog, promotes microtubule function in Caenorhabditis elegans neurons. eLife *3*. https://doi.org/10.7554/eLife.01498.

Rivadeneira, D.B., Caino, M.C., Seo, J.H., Angelin, A., Wallace, D.C., Languino, L.R., and Altieri, D.C. (2015). Survivin promotes oxidative phosphorylation, subcellular mitochondrial repositioning, and tumor cell invasion. Sci. Signal. *8*, ra80.

Rosado, C.J., Mijaljica, D., Hatzinisiriou, I., Prescott, M., and Devenish, R.J. (2008). Rosella: a fluorescent pH-biosensor for reporting vacuolar turnover of cytosol and organelles in yeast. Autophagy *4*, 205–213.

Salhi, A., Jordan, A.C., Bochaca, I.I., Izsak, A., Darvishian, F., Houvras, Y., Giles, K.M., and Osman, I. (2020). Oxidative phosphorylation promotes primary melanoma invasion. Am. J. Pathol. *190*, 1108–1117.

Schneider, C.A., Rasband, W.S., and Eliceiri, K.W. (2012). NIH Image to ImageJ: 25 years of image analysis. Nat. Methods *9*, 671–675.

Schwartz, A.B., Campos, O.A., Criado-Hidalgo, E., Chien, S., Del Álamo, J.C., Lasheras, J.C., and Yeh, Y.-T. (2021). Elucidating the biomechanics of leukocyte transendothelial migration by quantitative imaging. Front. Cell Dev. Biol. *9*, 635263.

Shah, N., Colbert, K.N., Enos, M.D., Herschlag, D., and Weis, W.I. (2015). Three αSNAP and 10 ATP molecules are used in SNARE complex disassembly by N-ethylmaleimide-sensitive factor (NSF). J. Biol. Chem. *290*, 2175–2188.

Sherwood, D.R., Butler, J.A., Kramer, J.M., and Sternberg, P.W. (2005). FOS-1 promotes basement-membrane removal during anchor-cell invasion in *C. elegans*. Cell *121*, 951–962.

Sherwood, D.R., and Sternberg, P.W. (2003). Anchor cell invasion into the vulval epithelium in *C. elegans*. Dev. Cell *5*, 21–31.

Shinoda, H., Shannon, M., and Nagai, T. (2018). Fluorescent proteins for investigating biological events in acidic environments. Int. J. Mol. Sci. *19*.

Smith, G.M., and Gallo, G. (2018). The role of mitochondria in axon development and regeneration. Dev. Neurobiol. *78*, 221–237.

Sturm, A., Saskoi, E., Tibor, K., Weinhardt, N., and Vellai, T. (2018). Highly efficient RNAi and Cas9-based auto-cloning systems for *C. elegans* research. Nucleic Acids Res *46*, e105. https://doi.org/10.1093/nar/gky516.

Sun, S., Liu, J., Zhao, M., Han, Y., Chen, P., Mo, Q., Wang, B., Chen, G., Fang, Y., Tian, Y., et al. (2017). Loss of the novel mitochondrial protein FAM210B

promotes metastasis via PDK4-dependent metabolic reprogramming. Cell Death Dis. *8*, e2870.

Tantama, M., Martínez-François, J.R., Mongeon, R., and Yellen, G. (2013). Imaging energy status in live cells with a fluorescent biosensor of the intracellular ATP-to-ADP ratio. Nat. Commun. *4*, 2550.

Urso, S.J., Comly, M., Hanover, J.A., and Lamitina, T. (2020). The O-GlcNAc transferase OGT is a conserved and essential regulator of the cellular and organismal response to hypertonic stress. PLoS Genet. *16*, e1008821.

van Spronsen, M., Mikhaylova, M., Lipka, J., Schlager, M.A., van den Heuvel, D.J., Kuijpers, M., Wulf, P.S., Keijzer, N., Demmers, J., Kapitein, L.C., et al. (2013). TRAK/Milton motor-adaptor proteins steer mitochondrial trafficking to axons and dendrites. Neuron *77*, 485–502.

Wang, L., Yuan, L., Zeng, X., Peng, J., Ni, Y., Er, J.C., Xu, W., Agrawalla, B.K., Su, D., Kim, B., and Chang, Y.T. (2016). A multisite-binding switchable fluorescent probe for monitoring mitochondrial ATP level fluctuation in live cells. Angew. Chem. Int. Ed. Engl. *55*, 1773–1776.

Wang, Z., Chi, Q., and Sherwood, D.R. (2014b). MIG-10 (lamellipodin) has netrin-independent functions and is a FOS-1A transcriptional target during anchor cell invasion in *C. elegans*. Development *141*, 1342–1353.

Wang, Z., Linden, L.M., Naegeli, K.M., Ziel, J.W., Chi, Q., Hagedorn, E.J., Savage, N.S., and Sherwood, D.R. (2014a). UNC-6 (netrin) stabilizes oscillatory clustering of the UNC-40 (DCC) receptor to orient polarity. J. Cell Biol. *206*, 619–633.

Wang, Z., and Sherwood, D.R. (2011). Dissection of genetic pathways in *C. elegans*. Methods Cell Biol. *106*, 113–157.

Wilson, D.F. (2017). Oxidative phosphorylation: regulation and role in cellular and tissue metabolism. J. Physiol. *595*, 7023–7038.

Wu, Y., Zanotelli, M.R., Zhang, J., and Reinhart-King, C.A. (2021). Matrix-driven changes in metabolism support cytoskeletal activity to promote cell migration. Biophys. J. *120*, 1705–1717.

Xing, R., Jin, Y., Sun, L., Yang, L., Li, C., Li, Z., Liu, X., and Zhao, J. (2016). Interleukin-21 induces migration and invasion of fibroblast-like synoviocytes from patients with rheumatoid arthritis. Clin. Exp. Immunol. *184*, 147–158.

Zanotelli, M.R., Goldblatt, Z.E., Miller, J.P., Bordeleau, F., Li, J., VanderBurgh, J.A., Lampi, M.C., King, M.R., and Reinhart-King, C.A. (2018). Regulation of ATP utilization during metastatic cell migration by collagen architecture. Mol. Biol. Cell *29*, 1–9.

Zhang, J., Goliwas, K.F., Wang, W., Taufalele, P.V., Bordeleau, F., and Reinhart-King, C.A. (2019). Energetic regulation of coordinated leader-follower dynamics during collective invasion of breast cancer cells. Proc. Natl. Acad. Sci. USA *116*, 7867–7872.

Ziel, J.W., Hagedorn, E.J., Audhya, A., and Sherwood, D.R. (2009). UNC-6 (netrin) orients the invasive membrane of the anchor cell in *C. elegans*. Nat. Cell Biol. *11*, 183–189.

STAR★METHODS

KEY RESOURCES TABLE

REAGENT or RESOURCE	SOURCE	IDENTIFIER
Bacterial and virus strains		
RNAi feeding strain	*Caenorhabditis* Genetics Center	HT115(DE3)
Vidal RNAi library	Open Biosystems	ORF RNAi Collection V1.1
Ahringer RNAi library	Source BioScience	*C.elegans* RNAi Collection (Ahringer)
Chemicals, peptides, and recombinant proteins		
Phloretin	Sigma Life Science	Cat. # P7912
2-deoxyglucose (2-DG)	Sigma Life Science	Cat. # D8375
Rotenone	EMD Millipore Corp.	Cat. # 557368
Levamisole hydrochloride	Millipore Sigma	Cat. # L9756
Mitotracker Red CMXRos	ThermoFisher Scientific	Cat. # M7512
Experimental models: Organisms/strains		
C. elegans wild-type strain N2	Caenorhabditis Genetics Center	WB Cat# N2_(ancestral). RRID: WB-STRAIN:N2_(ancestral)
C. elegans unc-119 injection strain; Genotype: *unc-119 (ed4)* III	Caenorhabditis Genetics Center	WB Strain
Wild-type strain with ratiometric ATP sensor PercevalHR Genotype *qyIs551* (*lin-29p::PercevalHR*)	this study	NK2627
Wild-type strain expressing AC specific cytoplasmic GFP Genotype *qyIs362* (*lin-29p::GFP*)	this study	NK1382
Wild-type strain expressing AC-specific cytoplasmic mCherry Genotype *qyIs17* (*zmp-1p::mCherry*)	Hagedorn et al., 2009	NK268
Wild-type strain with AC-specific membrane targeted GFP Genotype: *qyIs509* (*cdh-3p::GFP::caax*)	Naegeli et al., 2017	NK2099
ATGL:GFP reporter *hjIs67 (atgl-1p::atgl-1::GFP)*	Caenorhabditis Genetics Center	VS20
Uterine-specific RNAi strain with AC and BM markers for scoring invasion; Genotype *rrf-3 (pk1426)* II; *qyIs10* (*lam-1p::lam-1::GFP*) IV; *rde-1(ne219)* V; *qyIs24* (*cdh-3p::mCherry::PLCdPH*); *qyIs102* (*fos-1ap::rde-1, myo-2>GFP*)	Morrissey et al., 2014	NK1316
fgt-1 null mutant *fgt-1 (tm3165) II*	*C. elegans* Gene Knockout Consortium	FX18478
Wild-type strain with AC and BM markers for scoring invasion Genotype *qyIs23* (*cdh-3p::mCherry::PLCdPH*) II; *qyIs10* (*lam-1p::lam-1::GFP*) IV	Ziel et al., 2009	NK361
fgt-1 mutant with AC and BM markers for scoring invasion. Genotype *fgt-1 (tm3165) II; qyIs23 (cdh-3p::mCherry::PLCdPH) II; qyIs10 (lam-1p::lam-1::GFP)* IV	this study	NK2629
Wild-type strain with FGT-1::mNG knockin Genotype *fgt-1* (*qy65 [fgt-1::mNG]*) II	this study	NK2540
Wild-type strain with FGT-1::mNG expressed in the AC Genotype *qySi99* (*lin-29p::fgt-1::mNG*) I	this study	NK2632

(*Continued on next page*)

Continued

REAGENT or RESOURCE	SOURCE	IDENTIFIER
Wild-type strain with glucose biosensor Green Glifon 4000 expressed in the AC. Genotype *qyIs553* (*lin-29p::Green Glifon 4000*)	this study	NK2637
fgt-1 (*tm3165*) II; *qyIs551* (*lin-29p::PercevalHR*)	this study	NK2778
fgt-1 (*tm3165*) II; *qyIs553* (*lin-29p::Green Glifon 4000*	this study	NK2779
AC-specific PFK-1.1::mNG qySi564 (*lin-29p::pfk-1.1::mNG*) *I*	this study	NK2780
AC-specific PYK-1A::mNG qySi565 (*lin-29p::pyk-1a::mNG*) *I*	this study	NK2781
AC-specific ENOL-1A::mNG qySi566 (*lin-29p::enol-1a::mNG*) *I*	this study	NK2782
PYK-1A expressed under the *ced-10* promoter qySi567 (*ced-10p::pyk-1a::mNG*) *I*	this study	NK2783
wild-type strain with AC F-actin and BM markers. *qyIs50 (cdh-3p::moeABD::mCh) V; qyIs10 (lam-1p::lam-1:GFP) IV*	Hagedorn et al., 2009	NK439
fgt-1 (tm3165) II; qyIs50 (cdh-3p::moeABD::mCh) V	this study	NK2635
unc-6 (ev400) X; qy65 (fgt-1::mNG) II	this study	NK2794
unc-6 (ev400) X; *qySi99* (*lin-29p::fgt-1::mNG*) I	this study	NK2631
unc-6 (ev400) X; qyIs553 (*lin-29p::Green Glifon 4000*)	this study	NK2795
unc-6 (ev400) X; qySi564 (*lin-29p::pfk-1.1::mNG*) *I*	this study	NK2833
wild-type strain with TRAK-1::mNG knockin Genotype *qy158 (trak-1::mNG) I*	this study	NK2784
wild-type strain with AC microtubule marker Genotype: *qyIs570 (lin-29p::emtb::GFP)*	this study	NK2799
wild-type strain with AC mitochondria and F-actin markers Genotype *qyIs550 (zmp-1p::MLS::GFP); qyIs50 (cdh-3p::moeABD::mCh) V*	this study	NK2609
fgt-1 (tm3165) II; qyIs550 (zmp-1p:MLS:GFP); qyIs50 (cdh-3p:moeABD:mCh) V	this study	NK2639
wild-type strain with FGT-2::mNG expressed in the AC. Genotype *qySi569 (cdh-3p::fgt-2::mNG) I*	this study	NK2721
fgt-1 (tm3165) II; qySi569 (cdh-3p::fgt-2::mNG) I	this study	NK2785
MMP– [*zmp-1 (cg115); zmp-3 (tm3482); zmp-4 (tm3484); zmp-5 (tm3209); zmp-6 (tm3073)*]; *qySi569 (cdh-3p::fgt-2::mNG) I*	this study	NK2850
Oligonucleotides		
See Table S4 for details		
Recombinant DNA		
PercevalHR (*C. elegans* codon optimized)	Bohnert and Kenyon, 2017	Calico Labs pDONR221
Green Glifon 4000	Mita et al., 2019	Addgene (#126208); RRID: Addgene_126208
Green Glifon 4000 (*C. elegans* codon optimized)	this study	ceGlifon 4000
Rosella (*C.elegans* codon optimized)	this study	ceRosella
lin-29 promoter expression plasmid	this study	*lin-29bp::GFP::unc-54 3'utr*
unc-47p::pfk-1.1::GFP::unc-54 3'utr	Jang et al., 2016	Colón-Ramos Lab DACR 1851
unc-47p::pyk-1a::GFP::unc-54 3'utr	Jang et al., 2016	Colón-Ramos Lab DACR 2626
unc-47p::enol-1a::GFP::unc-54 3'utr	Jang et al., 2016	Colón-Ramos Lab DACR 2629

(*Continued on next page*)

Continued

REAGENT or RESOURCE	SOURCE	IDENTIFIER
T444T RNAi vector	Sturm et al., 2018	Addgene (#113081); RRID: Addgene_113081
trak-1 RNAi (in T444T vector)	this study	T444T- trak-1
fgt-2 RNAi (in T444T vector)	this study	T444T- fgt-2
Microtubule binding domain of ensconsin	Richardson et al., 2014	PCR8-EMTP::GFP entry vector
Mitochondrial import signal (MtLS) from Chicken Aspartate aminotransferase	Fire Lab Vector Supplement 1999	Addgene (Fire Vector, #1504); RRID: Addgene_1504
zmp-1p::mls::GFP::unc-54 3'utr	this study	*zmp-1p::mls::GFP*
Software and algorithms		
μManager	Edelstein et al., 2014	Version 1.4.23
Fiji	Schneider et al., 2012	Version ImageJ 1.52p
Imaris	Bitplane	Version 9.2
GraphPad Prism	GraphPad	Version 7
GPower	Faul et al., 2007	GPower 3.1
Excel	Microsoft	Version 2106
Illustrator	Adobe	Version CC 2020

RESOURCE AVAILABILITY

Lead contact

Further information and requests for resources and reagents should be directed to and will be fulfilled by the Lead Contact, David R. Sherwood (david.sherwood@duke.edu).

Materials availability

All worm strains will be available from the Caenorhabditis Genomics Center (CGC, gc.umn.edu).

Data and code availability

All raw data that were generated are available on request in a Dropbox file.

EXPERIMENTAL MODEL AND SUBJECT DETAILS

C. elegans strains were raised under standard conditions at 18°C or 20°C on standard NGM media and fed *Escherichia coli* OP50. N2 Bristol strain was used as wild type (Brenner, 1974). All animals scored and imaged were hermaphrodites during the L3 stage when the anchor cell (AC) invades. AC invasion was precisely staged in reference to vulval precursor cell (VPC) divisions and gonad development as previously described (Sherwood and Sternberg, 2003). Briefly, the AC becomes positioned over the central P6.p VPC at the early L3 stage prior to invasion. During the mid L3 stage, the P6.p divides once (P6.p 2-cell stage) and at the late P6.p 2-cell stage the AC initiates BM breaching. At the P6.p 2 to 4-cell stage (when the P6.p daughters divide) the AC forms a protrusion and clears an opening in the BM. Wild-type ACs complete BM removal by the early P6.p 4-cell stage (mid-to-late L3 stage) and the protrusion retracts back into the AC. L1 synchronization was performed by hypochlorite treatment. All alleles and strains used in this study are listed in key resources table and annotated according to WormBase guidelines: (https://wormbase.org/about/userguide/nomenclature#ecgkh5m87dlji1bf923a064–10).

METHOD DETAILS

Construction of transgenic strains

Worm strains expressing PercevalHR, Green Glifon 4000, mitochondrial localized GPF (*mls::GFP*) and ensconsin microtubule binding domain fused to GFP (*emtb::GFP*)in the AC were constructed as *unc-119* rescue integrated transgenes expressing multicopy arrays of the sensors (Sherwood et al., 2005). Worm strains expressing Rosella were constructed as lines expressing an extrachromosomal array. We found the ~1.5kb upstream regulatory region of *lin-29b* drove early and strong AC-specific GFP expression (pBlueScript *lin-29bp::GFP::unc-54 3'utr,* beginning ~4 hours prior to invasion at the P6.p 1-cell stage and throughout invasion*).* Thus, we used the *lin-29p* to drive most transgenes in the AC in this study. *lin-29p::PercevalHR::tbb-2 3'utr* was generated by directional cloning the following fragments in order: the linearized plasmid containing the *lin-29* promoter (*lin-29bp::GFP::unc-54 3'utr*), and PercevalHR::*tbb-2* 3'UTR, amplified from pDONR221 plasmid (see Table S4 for oligonucleotide sequences). *lin-29p::Rosella* was generating by Gibson assembling the following fragments in order, the linearized plasmid containing the *lin-29* promoter

(*lin-29bp::GFP::unc-54 3'utr)*, and Rosella amplified from a codon-optimized synthesized gene block (BioBasic). *lin-29p::Green Glifon 4000* was generated by Gibson assembling the following fragments in order, the linearized plasmid containing the *lin-29* promoter (*lin-29bp::GFP::unc-54 3'utr*), and Green Glifon 4000 amplified from a codon-optimized synthesized gene block (New England Biolabs). *zmp-1p::MLS::GFP* was generated by Gibson assembling the following fragments in order: the linearized plasmid containing *zmp-1p::GFP* (Kelley et al., 2019) and the mitochondrial localization signal (MLS) amplified from Fire Vector pPD96.32. *lin-29p::emtb::GFP* was generated by Gibson assembling the following fragments in order, the linearized plasmid containing the *lin-29* promoter (*lin-29bp::GFP::unc-54 3'utr*), and *emtb::GFP* sequence amplified from a PCR8 entry vector.

All four constructs were coinjected with 50 ng/ml *unc-119* rescue DNA, 50ng/ml pBsSK, and 25 ng/ml EcoRI cut salmon sperm DNA into *unc-119(ed4)* hermaphrodites. Multiple extrachromosomal lines with high transmission frequency were established and selected lines were integrated by gamma irradiation (Sherwood et al., 2005). Integrated lines were outcrossed to remove possible background mutations.

All other fusion proteins were generated via CRISPR-Cas9 mediated recombination to insert promoter driven translational reporters near the standard MoSCI insertion site ttTi4348 on chromosome I (Dickinson and Goldstein, 2016). Repair templates were made by Gibson assembly of protein coding sequences amplified from either genomic DNA or supplied plasmids (see key resources table for recombinant DNA and Table S4 for oligonucleotide sequences) into modular ttTi4348 directed plasmids containing *lin-29p::mNG, ced-10p::mNG, zmp-1p::GFP* or *cdh-3p::mNG*. For each strain, we injected 50ng/ml Cas9-sgRNA plasmid (pDD122), 100ng/ml repair template plasmid, and 2.5ng/ml pCFJ90 (*myo-2p::mCherry* as a co-injection marker) into the gonads of ~20-30 young adult N2 hermaphrodite animals and selection of edited lines was carried out as described previously (Al-Rekabi et al., 2017) and confirmed via observation of fluorescence.

Construction of Genome-edited Strains

To visualize endogenous protein levels, we used CRISPR-Cas9 mediated genome editing with a self-excising hygromycin selection cassette (SEC) based on previous methods and modifications (Al-Rekabi et al., 2017; Blanco and Blanco, 2017). Briefly, both *fgt-1* and *trak-1* were endogenously tagged at their C-termini, with mNG being inserted just before the stop codon. First, 2-3kb of DNA centered on the insertion site was amplified from N2 genomic DNA and cloned into an intermediate vector (TOPO) to be used as the template homology arms. Homology arms were mutated to introduce silent point mutations adjacent to the Cas9 cut site. Mutated homology regions were inserted into a repair plasmid using Gibson assembly. We generated one or two guide RNA (sgRNA) plasmids for each target by inserting the respective sgRNA sequences into the pDD122 plasmid. The sgRNA sequences used are listed (Table S4). Injections into animals and subsequent selection and excision were carried out as described (Dickinson and Goldstein, 2016; Keeley et al., 2020). Homozygous, wild-type animals with confirmed fluorescence signal were also PCR genotyped and the site of insertion sequenced to verify proper insertion.

Feeding RNAi

RNAi was delivered by feeding worms *Escherichia coli* strain HT115(DE3) expressing double-stranded RNA (Bonora et al., 2012). Bacteria harboring an empty RNAi vector (L4440 or T444T) was used as a control. RNAi clones originated from the *C. elegans* ORF-RNAi Collection V1.1 (Open Biosystems), an RNAi library constructed by the Ahringer lab (Brandina et al., 2006) or were generated in this study (Table S4).

RNAi bacterial cultures were grown in selective media for 12–14 h at 37°C, and then for an additional hour following addition of 1mM IPTG to induce double-strand RNA expression. 60mm nematode growth medium agar plates containing topically applied 1mM IPTG and 100-mg/ml ampicillin (5μl each) were then seeded with these RNAi bacterial cultures and left at room temperature overnight for further induction. Synchronized L1-arrested larvae were plated on the RNAi-expressing HT115(DE3) and grown for 36-42 hours at 18-20°C before scoring AC invasion at the L3 stage. The strain NK1316 was used for AC-specific RNAi experiments (Brenner, 1974; Bricker et al., 2012). NK1316 harbors mutations in *rrf-3* (*pk1426*), an RNA-directed RNA polymerase whose loss sensitizes the worms to RNAi, as well as *rde-1* (*ne219*), an argonaut protein required for RNAi. Expression of *rde-1* in the somatic uterine cells (*fos-1ap::rde-1*) specifically restores RNAi in the AC. The genome-scale RNAi screen used clones from the *C. elegans* Ahringer feeding RNAi library (Kamath and Ahringer, 2003). Synchronized *fgt-1* mutant L1 animals were plated on bacterial lawns of *Escherichia coli* expressing double stranded RNA, fed for 51 hours at 20°C in six-well plates, and screened for the presence of a protruding vulval (Pvl) phenotype using a dissecting microscope. 50–100 animals were examined per well and the number of Pvl animals recorded. The empty RNAi vector, L4440, was used as a control and an RNAi clone encoding *fos-1a*, which produces Pvl phenotypes following RNAi knockdown (Caino et al., 2015; Cambi and Chavrier, 2021), was used as a positive control. All RNAi clones that resulted in the presence of multiple Pvl animals (>5) and had no 'protruding vulva' annotation in Wormbase under 'Phenotypes' were re-screened alongside wild-type counterparts. Clones that had a high number of Pvl in *fgt-1* mutants and no Pvls in wild-type animals over two experiments were then scored for AC invasion defects (see Table S3). Following the initial RNAi screen, all clones that resulted in greater than 5 Pvls in *fgt-1* mutants were sequenced to verify their identity. For the three genes that were validated in the screen, *ogt-1*, *trak-1,* and *fgt-2,* we generated new RNAi clones in the more efficient T444T RNAi vector (Campanella et al., 2005) via Gibson assembly. Empty vector (T444T) was used as a negative control and RNAi against *fos-1a* in the T444T vector was used a positive control.

Microscopy and image acquisition

Most confocal microscopy images were acquired on a Zeiss AxioImager microscope equipped with a Yokogawa CSU-10 spinning disc confocal controlled by Micromanager software (Campanella et al., 2008) using a Zeiss 100x Plan-Apochromat 1.4NA oil immersion objective and a Hamamatsu Orca-Fusion sCMOS camera or ImageEM EMCCD camera. Additionally, a subset of PercevalHR analyses (Figure 6B) were acquired on a Zeiss 880 Airyscan point scanning confocal equipped with GaAsP QE32 detectors controlled by Zen 3.2 software using a Zeiss 63x Plan-Apochromat 1.4NA oil immersion objective.

For staging AC invasion, P6.p developmental stages were identified at 63x or 100x magnification in L3 larva collected from OP50 or RNAi plates and mounted onto 5% agar. Exposure times for confocal images varied based on fluorescence intensity. For time-lapse imaging of invadopodia and invasive protrusions and still images of fluorescent biosensors PercevalHR and Green Glifon 4000, worms were anesthetized in a solution of 5mM Levamisole for 30 mins and then mounted onto 5% agar pads, immobilized with 1μL undiluted 100nm polystyrene bead solution (CV 5%; Polysciences cat. #64010), the slide sealed with VALAP and imaged at 23°C. Additionally, for time-lapse imaging of invadopodia, animals were rolled ventrally as previously described (Kelley et al., 2017).

Stimulated Raman scattering (SRS) microscopy

For the SRS microscope system, pulsed Pump (tunable from 790 to 990 nm) and Stokes (1045 nm) beams were provided by Insight X3 femtosecond laser (Spectra-Physics), and spatiotemporally overlapped by a Spectral Focus Timing and Recombination Unit (SF-TRU, Newport). The intensity of Stokes beam is modulated at 20 MHz by an electro-optic modulator (EOM, 4103, New Focus). Overlapping pump and Stokes beams were emitted from the port of SF-TRU and coupled into a multiphoton laser scanning microscope (FVMPE-RS, Olympus). After passing through the sample, the forward going Pump and Stokes beams were collected by an air condenser. A flip mirror was used to direct the transmitted laser to a photodiode module, which includes a telescope to relay and change the beam size to fit the area of the photodiode, as well as an optical filter to remove the modulated Stokes beam and let the pump beam transmit for the detection of stimulated Raman loss signal. The output current from the photodiode was terminated, filtered, and demodulated by a lock-in amplifier (SRS Detection Module, APE) at 20 MHz to ensure shot noise-limited detection sensitivity. The lock-in amplifier output was then fed into the analog box of an FVMPE-RS microscope system to process the SRS signal. The microscope was controlled by Olympus Fluoview software. The AC was identified in mid-L3 larvae using a strain expressing AC-specific plasma membrane targeted GFP (*cdh-3p::GFP::caax*) using 2-photon imaging with the same microscopy setup, with the flip mirror flipped back to direct transmitted laser to photomultiplier tube detector. For lipid imaging, CH_2 signals were detected at 2845 cm^{-1} using a 60x water objective (UPlanSAPO, 1.2 N.A., Olympus). The pump beam was set at 805 nm. For the pump beam, 15-20% laser power was used, and for Stokes beam, 25% laser power was used.

Imaging PercevalHR

Images for PercevalHR ratiometric imaging to determine ATP:ADP ratio were acquired on a spinning disk confocal microscope using a 100x/1.4NA oil objective or a point scanning confocal using a 63x/1.4NA oil objective. PercevalHR contains an ATP binding protein GlnK1 fused to a cpmVenus fluorophore with two excitation peaks – 488nm wavelength corresponding to the ATP bound form of PercevalHR and 405 nm wavelength corresponding to the ADP bound form. Images were acquired for both excitation peaks using a common 525nm emission filter. PercevalHR ratiometric images were generated using the "Image Calculator > Divide" function in Fiji to divide the pixel values in the ATP channel with those in the ADP channel and are represented as spectral intensity maps of ATP channel/ ADP channel. The annotation of ATP:ADP for ratio follows previous references to this ratio (Tantama et al., 2013).

Imaging Rosella

Rosella consists of the pH insensitive red fluorophore DsRed expressed in tandem with highly pH sensitive green fluorophore super ecliptic phluorin (SEP, pKa 7.0). To image Rosella, confocal z-stack images were acquired on a spinning disk confocal using a 100x/1.4 oil objective using 488nm excitation and 525nm emission (SEP) and 561 excitation and 625nm emission (DsRed). Images are presented as 5-slice sum projections after background subtraction in Fiji (50 pixel rolling ball).

Imaging Green Glifon 4000

Green Glifon 4000 uses the green fluorescent protein Citrine. To image Green Glifon 4000 confocal z-stack images were acquired on a spinning disk confocal using a 100x/1.4 oil objective using 488nm excitation and 525nm emission. Images are presented as spectral representations of fluorescent intensity of a 5-slice sum projection after background subtraction in Fiji (50 pixel rolling ball).

2-deoxyglucose, Phloretin and Rotenone Treatment

60mm plates (Tritech Research #T3308P) containing 8mL of NGM and 1mM 2-deoxyglucose (2-DG or 2-DOG, Sigma Life Science Cat #D8375) were prepared. Synchronized L1 larvae were plated onto 2-DG plates with an OP50 food source and allowed to grow for 36-40 hours at 18° and 20°C until the L3 larval stage for AC invasion scoring as previously described (Sherwood et al., 2005). A phloretin stock of 10mM in DMSO was diluted to a working concentration of 75μM in 1mL of M9 and used to wash off synchronized early-to-mid L3 larvae (approx. P6.p 2-cell stage) from OP50 NGM plates and larvae were exposed to phloretin for 90 minutes at room temperature on a rocker. Animals were spun down and collected for AC invasion scoring. Control animals were treated with the same volume of DMSO in M9 for the same amount of time before scoring. A rotenone stock of 20mM in DMSO was diluted to a working concentration of 20μM in 1mL of M9 and synchronized early-to-mid L3 larvae were treated and scored as for phloretin treatment.

Staining with Mitochondrial Dyes

Mitotracker CMXRos (ThermoFisher Scientific #M7512) was reconstituted in DMSO to a concentration of 1mM and added to 60mm plates containing 8mL NGM to a final concentration of 250nM. Mitotracker CMXRos plates were then seeded with OP50 food for *C. elegans* culture. Synchronized L1 larvae were plated onto these Mitotracker CMXRos plates and allowed to grow in the dark for 24 hours at room temperature until the L3 larval stage for imaging. Biotracker ATP-Red 1 (Millipore Sigma SCT045) was reconstituted in DMSO to a stock concentration of 2mM and plated onto single wells of 6-well plates each containing 3mL of NGM to a final concentration of 10μM. Biotracker ATP-Red 1 plates was then seeded with OP50 bacteria. Synchronized L1 larvae were plated onto Biotracker ATP-Red 1 plates and allowed to grow in the dark for 24 hours at room temperature until the L3 larval stage. L3 larvae were moved from Biotracker ATP-Red 1 plates onto NGM plates seeded with OP50 for 20-30 minutes to clear excess dye signal from the gut lumen before imaging.

QUANTIFICATION AND STATISTICAL ANALYSIS

Analysis of Metabolic Biosensors

All measurements of fluorescence intensity were performed in Fiji 1.52p (Schneider et al., 2012). To measure ATP:ADP ratios by PercevalHR (Tantama et al., 2013) within the AC, we measured a region of interest encompassing the AC from a five-slice sum projection and then measured background fluorescence intensity outside the AC area. The final ATP:ADP ratio was determined by subtracting the value within the AC from the background value outside the AC. PercevalHR ATP:ADP invasive enrichment was calculated by measuring the ATP:ADP ratio in the basal cytoplasm (below the nucleus) and apical cytoplasm (above the nucleus) and determining the following ratio: [basal mean intensity – background]/[apical mean intensity – background]. Green Glifon 4000 invasive enrichment ratios were calculated from background subtracted (50 pixel rolling ball radius) z-stack images in Fiji by dividing the mean fluorescence intensity in the basal cytoplasm of the AC (below the nucleus) by the mean fluorescence intensity in the apical cytoplasm (above the nucleus).

Analysis of fluorescence enrichment in the AC and Invasive Membrane

For analysis of relative FGT-1::mNG and TRAK-1::mNG fluorescence levels in the AC compared to neighboring uterine cells, 5-slice sum projections of confocal z-stacks (with background subtraction, 20 pixel rolling ball radius) were used. For FGT-1::mNG, a 5-pixel wide line scan was used to measure the total signal on the plasma membrane of the AC and two uterine cells, and for TRAK-1::mNG a region of interest was drawn around the AC and two uterine cells and mean fluorescence intensity of each cell was then measured. Relative fluorescence intensity was calculated as the following ratio: [AC mean fluorescence intensity]/ [average of two uterine cells' mean fluorescence intensity]. AC invasive membrane enrichment of FGT-1::mNG and FGT-2::mNG were calculated using background subtracted 5-slice sum projections of confocal z-stacks by measuring the mean fluorescence intensity from a 5-pixel wide line scan drawn along the basal and apicolateral plasma membranes of the AC. Polarity was calculated using the following ratio: [basal mean fluorescence intensity]/[apicolateral mean fluorescence intensity].

Mitotracker CMXRos Invasive Mitochondrial Enrichment

To calculate the enrichment of Mitotracker CMXRos in invasive mitochondria near the basal invasive cell membrane compared to apicolateral mitochondria, background subtracted (20 pixel rolling ball radius) confocal z-stacks were used to draw a region of interest around individual mitochondrion. Two were randomly selected at the invasive side and two at the apical side for each AC at each developmental time point. The relative signal enrichment was calculated using the following ratio: [average of mean fluorescence intensities of basal mitochondria]/ [average of mean fluorescence intensities of apicolateral mitochondria]. Mitochondria were separated from large clusters of mitochondria for more accurate analysis.

Colocalization analysis

Colocalization analysis of glycolytic enzymes and mitochondrial signal was performed on confocal z-sections using the JACoP plugin in Fiji. Pearson's correlation coefficients (r) were calculated and compared from two regions of interest in each AC, the basal region (below the nucleus) and apical region (above the nucleus). Colocalization analysis of pH sensor Rosella's SEP and DsRed signal was performed on confocal z-sections using the JaCop plugin to calculate Pearson's correlation coefficients for the whole AC.

Invadopodia dynamics, F-actin volume, and Protrusion expansion

Invadopodia analysis was conducted using previously described methods for live cell imaging (Kelley et al., 2017). Briefly, AC invadopodia were visualized using the AC-expressed F-actin probe moeABD::mCh (*cdh-3p::mCh::moeABD*) in ventrally oriented animals and invadopodia dynamics (size and lifetime) were quantified using the Spots module in Imaris Version 9.2 (Bitplane). To measure F-actin volume, confocal z-stacks of ACs expressing the F-actin probe imaged laterally were used to generate 3D isosurface renderings in Imaris as previously described (Kelley et al., 2019). The renderings were created by setting a threshold that outlined the dense F-actin signal at the invasive surface. Quantitative measurement of isosurface volumes were then made to compare wild-type and *fgt-1* mutant ACs. Invasive protrusion volume and rates of expansion in time-lapses were measured by tracing the region of the protrusion that extended beneath the BM at each time point to generate a 3D isosurface rendering in Imaris as described (Naegeli et al., 2017). Images were acquired every five minutes for 90 minutes.

RNAi knockdown efficiency

To assess the knockdown efficiency of *trak-1, ogt-1,* and *fgt-2* RNAi (in the T444T vector), animals expressing endogenous *trak-1::mNG* and *ogt-1::GFP* or the *cdh-3p::fgt-2::mNG* transgene were plated onto empty vector control (T444T) and *trak-1, ogt-1* or *fgt-2* RNAi respectively, as synchronized L1 larvae and allowed to grow for 48 hours at 18°C until the L3 larval stage. Mean fluorescence intensity of TRAK-1::mNG, OGT-1::GFP and FGT-2::mNG in the AC were measured from background subtracted 5-slice sum projections of confocal z-stacks by drawing a region of interest around the AC in Fiji. Percent knockdown was calculated using the following formula: [difference between mean fluorescence intensity on the control plate and each RNAi plate]/ [mean fluorescence intensity on the control plate] x 100.

Spectral representation of fluorescence intensity

All spectral intensity maps of fluorescence signal were constructed to highlight fluorescence intensity differences of representative images shown in figures. These were generated using the 16-color lookup table (LUT) in Fiji and were displayed with a corresponding color bar. In data where all represented images were constrained to the same minimum and maximum pixel value ranges, these minimum and maximum pixel values were noted on the bottom and top of the color bar respectively. The variation in the values of minimum and maximum pixel value ranges in figures of PercevalHR are either due to the data being represented as normalized ATP:ADP ratios (as noted on the y-axes of the graphs and in the figure legends of Figures 1B and 6B) or being acquired on different microscope setups. In data where represented images were not constrained to the same minimum and maximum pixel value, color bars read hi and lo at the top and bottom respectively to denote the colors of the spectral map that represent high and low intensity pixel values.

Statistical analyses

For comparison of mean fluorescence intensity or invasive enrichment, either a pilot trial was conducted for each experiment and a priori power analysis was done to determine appropriate sample size (α: 0.05, β: 0.80) or a post-hoc power analysis was conducted to determine statistical power of the collected sample size (α: 0.05, β>0.80) using GPower 3.1. Each experimental data set was assessed for normality using a Shapiro-Wilk normality test. Statistical analyses were conducted, and all graphs generated in GraphPad Prism (Version 7). Statistical analyses comparing percent defective invasion in treatment conditions to control were conducted using Fisher's Exact 2x2 test. Comparisons of mean fluorescence intensity and invasive enrichment between a single condition and control were conducted using either an unpaired two-tailed t-test or an unpaired two-tailed t-test with Welch's correction when variances were different between the two groups based on an F-test. Comparisons of three or more conditions were done using a one-way ANOVA followed by a post-hoc Tukey's test. In box and whisker plots, box edges denote the 25th and 75th percentile, the line in the box is the median and the whiskers denote the minimum and maximum values of the dataset. Figure legends indicate sample sizes, statistical tests, and p-values. Experiments were not randomized and investigators were not blinded during analysis.